Is “expanded austenite” really a solid solution? Mössbauer observation of an annealed AISI 316L nitrided sample

T. Czerwiec, A. Andrieux, G. Marcos, H. Michel, Ph Bauer

Is "expanded austenite" really a solid solution? Mossbauer observation of an annealed AISI 316L nitrided sample

T. Czerwiec*, A. Andrieux, G. Marcos, H. Michel, Ph. Bauer

Institut Jean Lamour (IJL), Département CP2S, UMR 7198 CNRS, Université de Lorraine, 2 allée André Guinier, BP 50840, 54000 Nancy, France 2
Labex Damas, Nancy, France

* thierry.czerwiec@univ-lorraine.fr, phone + 33 3 72 74 24 98

ABSTRACT

Expanded austenite, also known as S phase, m phase or γ_N phase forms during low temperature (< 420°C) nitriding of austenitic materials containing chromium. In this communication, annealing of a nitrided sample is used as a tool to understand the nature of expanded austenite. Starting from an AISI 316LN sample plasma nitrided for 4 h. at 410 °C, the decomposition of expanded austenite is studied by conversion electron Mossbauer spectroscopy (CEMS) and X ray diffraction (XRD) for different annealing times at 400°C. For the as nitrided sample, the CEMS spectra are analysed using two hyperfine field distributions (HFD). HFD A is attributed to a nitrogen enriched expanded austenite, HFD B is attributed to a bcc environment without or with very low nitrogen content. Both the local deformation of the bcc lattice and the presence of other elements as iron neighbouring atoms explain the broad range of hyperfine field in HFD B. The vanishing of HFD A, after 2 h. of annealing, is explained by the formation of short-range order (SRO) between chromium and nitrogen and by the redistribution of nitrogen in excess. For the 3 h. of annealing, a bcc phase is observed by XRD. We propose to describe this phase as martensite. An interplay between local internal stress and local nitrogen content is proposed to explain the unexpected formation of such a martensitic phase in a strongly gamma stabilizing environment. From the microscopic point of view expanded austenite can be considered to be constituted of at least two different environments: a gamma environment supersaturated in nitrogen and a martensitic environment without nitrogen.

Keywords

Nitride materials, Surfaces and Interfaces, Mossbauer spectroscopy, gas solid reactions, X-ray diffraction, diffusion

1. Introduction

Austenitic stainless steels (ASSs) are steels with faced-centred cubic (fcc) crystal lattice containing a minimum of 16 wt% chromium and sufficient nickel and/or manganese to retain the austenitic structure at room temperature (with or without fast quenching depending on the composition). In the mid-1980s [1-2], two teams discovered that low temperature nitriding of austenitic stainless steels forms a new phase known as expanded austenite, S phase, m phase or γ_N phase. For the last thirty years, significant progresses have been made and now, it is more or less recognized that this phase is a metastable nitrogen supersaturated solid solution with a disordered fcc structure and a distorted lattice that will be called γ_N phase in this paper (figures 1a and 1b) [3-4]. However, some recent reports introduced a doubt on such a simple

description of expanded austenite [5-6]. The extended X-ray absorption fine structure spectroscopy (EXAFS) results from Oddershede et al. [5] show that short range ordering (SRO) of Cr and N atoms occurs (figure 1c). In this study, AISI 316 foils were nitrided at 445 °C in a 9% N_2- 91 % NH_3 (infinitely high nitrogen activity) for 18.5 h. From the authors, the nitrogen content is 33.8 at% and no Cr–N clusters (figure 1e) or CrN platelets or Guinier-Preston zones (figures 1f) are detected in such conditions. Using Field Ion Microscopy (FIM) Martinavicius et al. [6] observed small nanometric precipitates in AISI 304 samples treated by plasma nitriding at 400°C for 30 h. in a 60% N_2- 40 % H_2. These authors used the corresponding X-ray absorption near edge structure spectroscopy (XANES) and EXAFS data to describe expanded austenite as being constituted by nanometric precipitates, attributed to CrN, embedded in a Fe_4N-like matrix. The precipitates have irregular, sphere-like shapes with larger size near the surface. X-ray spectroscopic investigation revealed three different intermetallic distances and different chemical environments for Fe, Cr and Ni, accompanied by a large disorder. However, these authors were not able to evidence CrN precipitates by atom probe tomography. Some transmission electron microscopy (TEM) measurements done on low temperature nitrided stainless steels do not support the simple description of expanded austenite as a solid solution [7-8]. Xu et al. have analysed by TEM AISI 304 samples plasma nitrided in the range 400-420 °C in NH_3 for 4 h. [8]. They describe expanded austenite as being constituted by a supersaturated nitrogen solid solution based on a γ'-Fe_4N structure, in which the nitrogen atoms are in the form of Cr–N clusters. From high resolution TEM measurements, Strotz et al. [9] concluded that only the S-phase is formed in AISI 316L stainless steel plasma nitrided for 4 h. at 440°C in 50% N_2 -50% H_2 gas mixture. However, they suggested a tendency to short-range ordering of γ' Fe_4N type in a supersaturated solid solution of nitrogen. It was suggested that SRO of nitrogen atoms takes place and gives rise to appearance of forbidden {100} reflections from γ'.

Unlike the paramagnetic austenite phase of the matrix, expanded austenite containing nitrogen is known to be ferromagnetic at room temperature [10-13]. Nevertheless, relatively little is known about the magnetic properties of expanded austenite. Such magnetic properties make backscattered conversion electron Mossbauer spectroscopy (CEMS) an interesting technique for studying expanded austenite since it provides information on backscattered electrons with an average escape depth of about 60 nm (80% are from the range 0-0.1 μm) [14].

In order to better understand expanded austenite, it can be useful to destabilize this phase by annealing at a temperature used for the nitriding treatment. It is important to remember that the migration of metal constituents during a low temperature nitriding treatment (< 420°C) for relatively short treatment times (few hours) is practically zero, while migration of nitrogen atoms occurs. The term paraequilibrium is sometimes used to characterize such a state of metastability whereby equilibration of the chemical potentials of carbon or nitrogen in solution with the atmosphere occurs, but not those of metal constituents [15-16]. As nitrogen is continuously supplied into expanded austenite during a nitriding treatment, its metastable nature is hindered. The situation is different when the nitrogen supply is suppressed during annealing. The purpose of this paper is to study expanded austenite through CEMS by following the evolution of a nitrided layer during several annealing steps.

2. Experimental

The sample used in this communication is a tempered AISI 316LM stainless steel cylinder (14.7 wt% Ni, 17.4 wt% Cr, 62.7 wt% Fe, 2.7 wt% Mo, 1.8 Mn, 0.4 wt% Si, 0.2 Cu, wt% …) cut from a cylindrical rod (20 mm of diameter) and with a thickness of less than 5 mm. The sample was mechanically polished to a mirror-like finish and cleaned in ethanol for 15 min. using ultrasonic cleaning just before being placed into the nitriding chamber. A multi-dipolar

electron cyclotron resonance system (MDECR) was used for the nitriding experiments [17]. An in-situ cleaning pre-treatment, intended to remove the native oxide layer, was performed in 50% Ar-50% H_2 at a pressure of 1 Pa for 20 min. For this step, the incident microwave power was 600W and the bias voltage is -200V. The plasma was maintained in between the pre-treatment and the nitriding treatment to reach the treatment temperature. Additional heating of the substrate is provided by external heating integrated to the substrate holder. The temperature of the sample was controlled with a thermocouple embedded in the substrate holder. The nitriding treatment was performed in 90% N_2-10% H_2 at a pressure of 1 Pa for 4 h. with an incident microwave power of 600W and a bias voltage of -50 V. Annealing were sequentially done in the nitriding chamber without plasma and under secondary vacuum (< 10-3 Pa) for different times. After each set of annealing, the sample was allowed to cool in the reactor under vacuum at room temperature before both X-ray diffraction and CEMS measurements.
X-ray diffraction analysis was done using a Ge monochromator (111) to discriminate copper $K_{\alpha 1}$ line (λ = 0.154056 nm) in the Bragg-Brentano type configuration (Brukers Advance diffractometer). The sample is positioned in the center of the goniometer on a spinner by an automated smuggler. We used the EVA software to subtract the background noise and to extract the characteristic data of the diffraction peaks. Glow Discharge Optical Emission Spectrometry (GDOES) measurements were performed using a Jobin-Yvon Horiba GD 1000 apparatus. A dedicated and calibrated method for these types of samples (nitrided iron-base) has been developed. It takes into account all the alloying elements. For the determination of nitrogen concentration, a calibration curve was carried out using a series of certified samples containing a wide range in nitrogen concentration (10^{-5} to 22.633 % Wt). For recalibration or pre-measurements, a sample of nitrided pure iron sample (pure γ'-Fe_4N phase controlled by X-rays diffraction) is routinely used. All calibration curves and measurements were made under the same operating conditions of the Grimm lamp (650 Pa of pressure, 30 W of RF power). We have verified with tactile profilometry that with these parameters the craters have an adequate shape (anisotropic sidewalls and flat bottom) for a good resolution (50 nm) monitoring of the concentrations with the depth.
Room temperature 57Fe Mossbauer spectroscopy using both backscattered conversion electron (CEMS) was performed using a conventional spectrometer operating in constant acceleration mode. The detection of the backscattered conversion electrons was made using gas flow proportional counter (He -5% CH_4). The Mossbauer spectra exhibit magnetic Zeeman patterns with six broadened lines superimposed to a central paramagnetic component. The magnetic contribution arises from the existence of distributions of hyperfine magnetic fields B. In order to analyze our Mossbauer spectra, we use the method developed by Le Caer and Dubois [18] for amorphous alloys, which is an improvement of that proposed by Hesse and Riibartsch [19]. The hyperfine field distributions (HFD) method assumes a linear correlation between the hyperfine field and the isomer shift δ in order to take into account the Fe-environment distribution. It gives probability curves p(B). This type of correlation is justified because the isomer shift is directly proportional to the total s-electron density at the nuclear site. A change in HFD is due to a change in the spin-up or spin-down s-electron density which also modifies the total s-electron density and hence the isomer-shift proportionally [20].

3. Experimental results

Figure 2 represents the CEMS spectrum of a non nitrided AISI 316L sample. A single line, associated to a paramagnetic (see table 1) is observed in this figure. CEMS spectra, performed on the same sample nitrided for 4 h. at 410° C and then annealed for different conditions are

presented in figure 3. The CEMS spectrum of the nitrided sample without annealing exhibits 2 kinds of magnetic components superimposed to a paramagnetic contribution. This last paramagnetic contribution, fitted with a lorentzian line shape, is attributed to an austenitic environment. The two major broad components exhibited by the CEMS spectra are analysed using hyperfine field distributions (distributions A and B) with linearly correlated isomer shifts (formerly known as smoothed histogram method). However, the histograms of the two distributions defer markedly.

HFD A is nearly Gaussian and is associated to expanded austenite with magnetic characteristics (called γ_N(m)) as proposed by Williamson et al. [21]). These authors characterized the CEMS spectra either by a hyperfine field distribution or by a fit of six broadened Lorentzian lines (average field 15-16 T). In our case, the average magnetic field is 20-21 T. The origin and possible interpretation for HFD A will be discussed later. An interpretation of HFD B will be presented in the discussion of this paper.

The CEMS spectrum recorded after 1 h. of annealing at 400°C (figure 3 b) shows a decrease of the contribution from HFD A. After 2 h. of annealing at the same temperature, HFD A is not necessary to describe the CEMS spectra (figure 3c). Only HFD B and the paramagnetic contribution must be used to fit the data. The magnetic field and hyperfine parameters of distribution B are practically unchanged. It must be noted that it is necessary to include additional Zeeman sextets with high magnetic fields to describe HFD B after 2 h. of annealing. For 3 and 8 hours of annealing (figure 3d and e), some iron oxides (Fe_2O_3) are detected in the CEMS spectra. The CEMS spectra resulting from the final step of annealing, additional 5 h. at 470 °C (figure 3f) can be described by three simple components without the need of HFDs. An austenitic environment contributes to 47% of the total signal, and two magnetic contributions at 34.3 T and 33.3 T with a respective proportion of 15% and 28%. The lowest magnetic contribution is characterized by a perpendicular anisotropy.

GDOES profiles of nitrogen content, performed on the same sample nitrided for 4 h. at 410° C before annealing and after annealing, are presented in figure 4. It can be seen that the layer thickness of the nitrided sample lies between 7.5 to 8 µm and that the surface content in nitrogen is around 25 at%. The nitrogen content profile has the classic form found in low temperature nitriding experiments of austenitic stainless steels [3-4]. Some models were proposed to explain such nitrogen profile (see reference [22] for more details). It is necessary to include composition-dependent diffusion coefficient of nitrogen in expanded austenite, short range ordering (trapping) of nitrogen atoms by chromium atoms, and the effect of composition-induced stress (elastic and plastic) on surface concentration and diffusive flux [22]. At the end of the annealing process, the superficial nitrogen content decreases to 17.5 at% and the thickness of the layer containing nitrogen reaches 11.5 to 12 µm. After annealing, the shape of the nitrogen profile is even more complex to describe than before annealing. It will be interesting to model such a profile. Nevertheless, the integral over the nitrogen profiles (total nitrogen content into the sample) respectively gives 95 and 87 at%.µm before and after annealing. Approximately 8 % of the nitrogen atoms initially incorporated in the nitrided sample are lost during the annealing process. The loose of nitrogen can be explained by nitrogen atoms recombination at the sample surface [23]. The insert in figure 4 represents the depth profile of the difference between the measured nitrogen and chromium contents.

The corresponding X-ray diffraction (XRD) patterns are shown in figure 5. From this figure the characteristic set of diffraction lines corresponding to the γ_N phase can be recognized for the nitrided sample. Each diffraction line from the γ phase substrate is associated to a diffraction line from the γ_N phase appearing at lower angles. Additional lines with low intensity appear in the XRD pattern of the as nitrided sample. The line at 38.29° cannot be identified. It does not correspond to any nitrides or any sulphides. The line at 44.7° (depicted by a star in figure 5) is difficult to interpret but the presence of ferrite is not completely

excluded (possible lattice parameter 0.286 nm). After 2 h. of annealing, a new line attributed to a bcc structure appears in the XRD pattern, while the (200) line of the γ_N phase disappears. It is not the case for the (111) line attributed to the γ_N phase. For 8 h. of annealing, a new diffraction line appears. It is attributed to an fcc phase, called decomposition austenite γ_d because its appearance is linked to the disappearance of the γ_N phase. Finally, we are able to identify the XRD line belonging to CrN only at the end of the annealing process. Figure 6 represents the evolution of the lattice parameters calculated using the previously presented assumptions. Concerning the diffraction lines of the γ_N phase, a linear decrease is observed for both the (111) and the (200) lattice parameters. The anisotropic behaviour is explained by the anisotropy of the elastic constant of stainless steel and by the very high compressive internal stress observed in such nitrided layers [3]. Despite the fact that the (200) line cannot be observed for annealing times higher than 2 h., we can extrapolate the linear behavior of two lines to determine a theoretical annealing time of 4 h. for which the anisotropic behavior disappears. From our GDOES measurements, it can be seen that the superficial nitrogen content decreases with the annealing time. The decrease of the lattice parameters of γ_N is explained by a combination of internal stress and superficial nitrogen content decrease.

4. Discussion

4.1 Before annealing: origin of HFD A

Mossbauer studies concerning the effect of nitrogen on iron in austenite at low nitrogen content (less than 10 at%) are well documented in pure iron or in stainless steels [24-29]. With such low nitrogen content, two kinds of components are observed in the Mossbauer spectra of ^{57}Fe: a singlet which is assigned to iron atoms having no nearest interstitial atoms and a doublet assigned to those having interstitial atoms at the nearest neighboring sites. A quadrupole splitting of resonance lines due to a breaking of symmetry of the electronic charge distribution near Fe atoms by the nearest interstitial nitrogen neighbor occurs. It was described as a paramagnetic austenite $\gamma_N(p)$ with two subcomponents γ_1 and γ_2. The isomer shift increases with nitrogen interstitial content as a result of a decrease of the s electron charge density. Williamson et al. [21] were the first to interpret the Mossbauer results obtained on austenitic stainless steels containing high nitrogen content (up to 30 at%) as being due to a ferromagnetic state of austenite (called $\gamma_N(m)$). Using secondary neutral mass spectrometry combined to magnetic force microscopy image, it was shown that γ_N can be found in two different magnetic states depending on the position in the nitrided layer [13]. An outermost ferromagnetic layer is found for nitrogen content higher than 14 at% (associated to $\gamma_N(m)$ in [21]) while a paramagnetic layer (associated to $\gamma_N(p)$ in [21]) lying beneath $\gamma_N(m)$ is observed for nitrogen content lower than 14 at%.

The $\gamma_N(p)$ environment was not observed in our experiment, contrary to ref. [21], probably because the layer thickness of our sample is higher: 7 µm as compared to 1.4 µm in ref. [21]. From figure 4, it can be seen that the transition region (between $\gamma_N(m)$ and $\gamma_N(p)$) lies between 3.5 to 4 µm in the present experiment, fare away from the first hundreds of nanometres probed by CEMS. This explain why it is not possible to see any contribution from $\gamma_N(p)$ in our experiments. As the isomer shift of the paramagnetic component from our CEMS spectra is -0.1 m.s^{-1}, it can be concluded that it is associated to an austenitic environment of iron without nitrogen interstitials. It should be noted that Williamson et al. [21] also observed such an austenitic environment in AISI 304 stainless steel implanted at 400°C for 30 min. resulting in 1 to 2 µm nitrided layers. They attributed this component to the signal coming from the substrate, despite the fact that CEMS is mainly sensitive to the first hundreds of nanometers

from the top surface. We believe that this gamma phase without nitrogen is the result of a decomposition mechanism that will be discussed in the second part of this discussion.

HFD A must be associated to the ferromagnetic state of expanded austenite called γ_N(m). Cusenza et al. [30] have obtained AISI 316 films enriched in nitrogen by reactive magnetron sputtering in argon-nitrogen gas mixtures. They were using an HFD, very similar to the one we use, in order to interpret the CEMS obtained on low nitrogen containing films (< 30 at%). The mean magnetic field of this contribution, which was between 23.4 and 18.2 T depending on the conditions, was attributed to an amorphous stainless steel nitrogen alloy. Brink et al [31] also used two HFD to describe the Mossbauer spectra measured on fully expanded austenite samples obtained by foils nitriding. The mean magnetic field was between 18 and 19 T for IS of 0.33, 0.37 mm. s^{-1} for nitrogen content 25 to 30 at%. Olzon-Dionysio et al. [12] also analyzed CEMS spectra obtained on AISI 316L samples nitrided at 400°C from 1 h. using two magnetic components with magnetic field of 19.9 T (IS = 0.16 mm. s^{-1}) and 15.4 T (IS = 0.07 mm. s^{-1}). It must be noted that these authors used other magnetic phases to fit the CEMS for longer nitriding times: γ′-Fe_4N (three components, magnetic field of 33.6, 21.5 and 21.1 T for IS of 0.29, 0.22 and 0.25 mm. s^{-1} respectively) and ε-$Fe_{2+x}N$ (26.4 T and 0.23 mm. s^{-1} respectively). Recently, these authors introduced an HFD in their analysis of AISI 316 L nitrided samples analysis together with γ′-Fe_4N and ε-$Fe_{3+x}N$ components [32]. It is tempting to interpret HFD A as resulting from a deformed Fe_4N cubic structure. As a matter of fact, Fe_4N can be described as an anti-perovskite structure with two different Fe sites: Fe I atoms occupy the corners of the cubic unit cell and are surrounded by 12 nearest neighbours and Fe II atoms occupy the face centres of the unit cube and have two nitrogen atoms as nearest neighbours (respectively M in position I and M in position II on figure 7). Nitrogen occupies the body centre and the structure can also be considered as a γ-Fe where nitrogen is at the body centred position [33-34]. The ferromagnetic nature of γ' has an influence on the Mössbauer spectra giving quadrupole splitting due to combined magnetic and electric hyperfine interactions. As a consequence of the orientation of the internal magnetic field along the easy magnetization direction, crystallographically equivalent sites are magnetically non-equivalent (MIIA and MIIB in figure 7). For γ'-Fe_4N, the hyperfine parameters are, at room temperature, 34.1-34.4, 21.7-22 and 21.8-21.9 T for the hyperfine field and 0.22-0.23, 0.29-0.3 and 0.29-0.3 mm. s^{-1} for the IS, respectively for Fe I, Fe IIA and Fe IIB [33,35]. Note that the results are different at low temperature [34]. A direct comparison shows that HFD A has a too much broad range of hyperfine fields to be identified to γ'-Fe_4N. Nevertheless, it must be emphasized that the maximum hyperfine field of HFD A is not so far from the hyperfine field of site Fe IIA from γ'-Fe_4N. Both calculations [36, 37] and experimental studies [38, 39] on the effect of pressure on the hyperfine parameters of γ' Fe_4N, show that a compressive state of stress, that results in a contraction of the lattice, reduces the hyperfine field and the IS of both Fe I and Fe II. The reverse holds for a tensile state of stress that expands the lattice. From the experimental data obtained at room temperature of Li et al. [39], the hyperfine field vary from 34.3 to 29.8 T (Fe I) and 21.9 to 19.4 T (Fe II) whereas the IS is not changing for Fe I (0.3 to 0.22-0.23 mm. s^{-1}) and vary from 0.3 to 0.26 mm. s^{-1} for Fe II as the pressure increases from 0 to 5.6 GPa. Such observations can only partly explain our results but not the very broad range of hyperfine field of HFD A around its maximum. As AISI 316 L also contains nickel, some γ'-$(Fe_{1-x}Ni_x)_4N$ can be formed during nitriding. The hyperfine parameters were measured for different compositions of γ'in which nickel is substituted to iron [34-35, 40]. All the authors observe an increase of the hyperfine field for Fe I from x = 0 to x = 0.4; the other hyperfine parameters were not so much affected by a change in the nickel content. The presented results are different for x > 0.4: the contribution from Fe I disappears for Diao et al. [34], decreases for El Khiraoui et al. [40] or stabilizes for Panda et al. [35]. Note that these last authors used HFD to describe the internal fields because

of the alteration of the local environment. Again, taking into account nickel substitution to iron in γ'cannot explain the very broad range of hyperfine field of HFD A. However, one interesting point to consider is the disappearance of the contribution from Fe I as γ' is enriched in nickel. "Given the comparison of our results with those of the literature, the distribution A must be attributed mainly to expanded austenite".

4.2 Before annealing: origin of HFD B

In order to interpret HFD B, we had to discuss the role of nitrogen on the isomer-shift of iron in different structures. From the results presented before for the γ and γ' structures, it results that the presence of nitrogen near iron is characterized by high values of isomer-shift (typically 0.2 to 0.3 mm. s^{-1}). So HFD B cannot be interpreted as such type of environment that contains nitrogen. It corresponds neither to a $\gamma_N(p)$ or $\gamma_N(m)$ nor to a γ' structure. Schaeffler or Delong diagrams show that AISI 316 is a metastable austenitic steel, mostly stabilized by fast quenching from the liquid state during elaboration [41]. Shabashov et al. [42] performed electron beam plasma nitriding of austenitic stainless steels with lower Ni content (7-9 at%) as content as compared to AISI 316L. The formation of α' martensite was reported in surface after short time nitriding at 350°C [42]. An HFD, similar to the one reported here but with lower hyperfine fields (maximum for 27 T), was used to describe the α' martensite obtained by nitriding. Shabashov et al [42] justified this interpretation by comparing the HFD attributed to martensite obtained by nitriding and by high pressure torsion. In this study, it is clearly shown by successive removal of the nitrided layer, that the α martensite HFD observed in surface is different from the HFD resulting from γ′-Fe_4N and ε-$Fe_{2+x}N$, observed deeper. It is well known that layers formed by PVD deposition of austenitic stainless steels are, most of the time, constituted by a bcc phase [43-46]. In all these works, the authors use HFDs to describe the structure observed by Mössbauer spectroscopy. For AISI 316L films elaborated at 450°C, the used HFD is very similar to HFD B reported here [46]. Some authors reported the formation of martensite in AISI 316 steels using different process: ion implantation (nitrogen and other elements), severe mechanical deformations, hydrogen absorption… [47-57]. Two types of martensite can form in stainless steels: martensite α' (a ferromagnetic body centered cubic structure) and martensite ε (compact hexagonal structure which is not ferromagnetic). After 40 keV helium ions bombardment on AISI 316, Hayashi et al. [47] observed by CEMS a ferromagnetic phase they attributed to martensite. Three components were used to fit the spectra with respective isomer-shift of 0.05, - 0.02 and 0.05 mm. s^{-1} corresponding to hyperfine field of 27.8, 30.3 and 33.4 T. Mottu et al. [48] observed ferrite by XRD during implantion of Xe and Mo ions at 49 keV at doses higher than 6 10^{15} ions. cm^{-2}. Dudognon et al. [49] showed that the formation of ferrite does not depend on the nature of the implanted dose or elements, but rather on a threshold for the development of damage in the material. Referring works on the formation of martensite induced by deformation (deformation induced martensite: DIM) are relatively few with respect to AISI 316. Cook [50] observed martensite formation on AISI 316 samples deformed by brushing using CEMS. In this paper, an HFD, very similar to HFD B reported here was used to describe the Mössbauer spectra [49]. Varma et al. [51-52] observed martensite in AISI 316L during mechanical rolling tests, but not during tensile tests. Martensite was also observed in AISI 316 L by TEM on wires deformed by cold drawing [53]. Szymańska et al. [54] observed martensite by XRD and Mössbauer spectroscopy after powder grinding of AISI 316. When AISI 316 is previously subjected to neutron bombardment, the formation of martensite is observed during tensile tests [55]. Manjanna et al [55-56] showed that martensite is formed during compression tests on AISI 316LN. Menendez et al. [58-59] observed martensite by magneto-optical Kerr effect and magnetic force microscopy on indented AISI 316L samples. Etienne et al. [60] observed by XRD and Mossbauer spectroscopy the formation of α'

martensite on very fine grained samples prepared by high pressure torsion from AISI 316. During cathodic charging of hydrogen (electrochemical solution method), Rozenak et al. [61-62] observed by XRD ε and α' martensite. It is interesting to note that a duplication of the γ diffraction peaks is attributed to the effect of internal stresses induced by the introduction of hydrogen into the steel [61-62]. We will now look at the role of nitrogen on the isomer-schift in martensite. Genin and Foct [24] distinguished four different environments for iron martensite as respect to nitrogen: class A* in which Fe atoms have no nitrogen within the first and second nearest neighbour shells (nn and nnn respectively), class A' in which Fe atoms have no nn nitrogen but one nitrogen nnn, class B includes iron atoms which have one isolated nitrogen nn, and finally class C* in which Fe atoms are close to several nitrogen atoms. A very weak isomer shift is found for classes A* and A' (about 0.04 mm. s^{-1}) since Fe atoms ignore the presence of the interstitial except through the conduction band of iron. The values for class B is $\delta = 0.40 \pm 0.05$ mm. s^{-1}. Such a positive value reveals a decrease of the s-electron density attributed to a more effective 3d screening effect. The isomer shift is found to be $\delta = 0.23$ mm/s for class C*. By comparing our results to those coming from the literature, it appears that HFD B must be attributed to a bcc environment with no or with very low nitrogen content. The broad range of hyperfine field in HFD B can be explained by both the local deformation of the bcc lattice and by the presence of Cr, Ni, Mo… elements as iron neighbouring atoms. It was shown that the hyperfine field experienced by a given Fe atom depends on the number and distance of Fe and non-Fe neighbouring atoms. Due to the reduction of the exchange interaction by each non-Fe nn and next-nearest neighbour (nnn) atom, the hyperfine field decrease is proportional to the numbers of nn and nnn foreign atoms [60]. So a martensitic environment with very low or no nitrogen content can be a good candidate to explain HFD B.

4.3 Annealing

First of all we have to discuss the fact that HFD A does not longer exists for annealing times higher than 2 h. It is remarkable to note that this event occurs simultaneously with the appearance of the bcc phase and the vanishing of the γ_N (200) peak as observed by XRD (figure 6). As the nitrogen gas supply stops during the annealing process, nitrogen atoms will continue to diffuse from the superficial part of the nitrided layer into the steel. Thus, the nitrogen content in the superficial layer decreases and, in spite of the γ stabilizing effect of nitrogen, the stainless steel-nitrogen system will tend to an equilibrium state producing CrN, a bcc phase (and a fcc phase if the temperature is high enough). The experimental data concerning the stability of expanded austenite are scare [63-67]. In a first approach, Li et al. have obtained isothermal transformation (IT) diagrams from annealing and TEM in-situ heating observations [63]. The transformation time was found to be temperature dependent, ranging from several minutes at 600°C or over to a couple of years at 300°C or below. From the examination of these data, it appears that the decomposition time at a given temperature is strongly dependent on the initial state of expanded austenite (nitrogen content, thickness, treatment time…). In our experiment, it is surprising that the first stage of the decomposition process appears very early, after 2 h. of annealing at 400°C. As indicated by GDOES measurements, the maximum amount of nitrogen in the nitrided layer corresponds to the amount of chromium at the end of the annealing procedure. The insert in figure 4 shows the evolution of the difference between the nitrogen and the chromium content as a function of depth. This value is almost zero at the end of the annealing procedure, but it can be as high as 10 at% for the nitrided specimen. At the end of the annealing procedure, the combined observations of the 1:1 ratio of chromium and nitrogen, as well as the appearance of CrN diffraction lines, leads us to believe that the thermodynamic equilibrium tends to be established within the nitrided layer (figure 1e). Nevertheless, it very likely that the 1:1

interaction between Cr and N occurred earlier in the annealing procedure and also during the nitriding treatment itself. Indeed, SRO of Cr and N (figure 1c) is probably present at the early stage of nitriding in AISI 316L. Nitrogen atoms not strongly linked to chromium by SRO, can be considered as nitrogen atoms in excess. According to our Mossbauer measurements, these nitrogen atoms in excess are at the origin of HFD A and must be located near the chromium atoms, but are not strongly linked to chromium compared to the nitrogen atoms in SRO (figure 8). These excess nitrogen atoms are almost free to diffuse during annealing, but also during nitriding treatments. We are able to distinguish nitrogen atoms in excess from those involved in SRO only by performing annealing experiments. We believe that the vanishing of HFD A after 2 h. of annealing is related to the redistribution of these excess nitrogen atoms. Nitrogen atoms are associated to an enormous γ stabilizing effect. However, they are located near chromium atoms and the consequence is the appearance in the nitrided samples of zones mostly containing iron atoms with no nitrogen atoms within the first and the second neighbour shells. Such an iron environment without nitrogen can be associated to HFD B (figure 8). A similar, but different approach was proposed by Jack et al. [68-70] within the frame of titanium nitrogen interaction in a ferritic environment. In this model, titanium-nitrogen atom clusters form one dimensional Guinier-Preston zones (figure 1g). The formation of SRO between chromium and nitrogen is associated to distortions producing expansion and contraction of the atomic spacing around the chromium atoms as suggested by Oda et al. [28]. Such distortions explain that distributions are required for the interpretation of the Mossbauer spectra.

The occurrence of higher hyperfine magnetic field in HFD B for annealing times higher than 2 h. can be interpreted as a reordering of the bcc environment in favour of iron as neighbour of iron. The fact that the (200) line of γ_N disappears before the (111) line is interesting to discuss. Brink et al. [67] observed a low nitrogen content gamma phase (named γ_T) by *in-situ* synchrotron XRD experiments during annealing experiments on low and high nitrogen content expanded austenite. Such an observation seems to be connected with our finding. In order to try to explain the persistence of the γ_N (111) line, we had to take into account the highly anisotropic character of both the elastic and plastic strains induced by internal stress in expanded austenite [3, 71]. It was shown that the strain perpendicular to the sample surface is higher for (200) grains as compared to (111). It can be postulated that the deformation in (200) grains of expanded austenite is high enough to promote the formation of martensite by a Bain distortion scheme [72], while it is not in (111) oriented grains. Following this hypothesis, the bcc phase observed by XRD must be attributed to martensite, probably located in the (200) oriented grains at the early stage of the decomposition. Such a transformation mechanism is only able to occur if a certain amount of excess nitrogen, which stabilizes austenite, is locally removed from the superficial layer. A balance between the local internal stress, which decreases when the nitrogen content decreases, and the local nitrogen content, which stabilize austenite, must be reached in order to allow the formation of martensite. From our CEMS experiments, it can be deduced that a martensitic environment is initially found in the nitrided layer. The occurrence of a bcc phase, as detected by XRD after 2 h. of annealing, is connected to HFD B, a martensitic environment of iron with low nitrogen content or without nitrogen.

A second interesting point to discuss is the evolution of the lattice parameter from the bcc phase observed by XRD (figure 6). The lattice parameter for α iron is between 0.2866 and 0.2868 nm [68-69], and is around 0.287 nm for α' in Fe-10 to 20 wt% Ni [73]. The lattice parameter from our bcc phase is higher than these values, but not high enough to be associated to ε martensite containing nitrogen. Indeed, c values starts from 0,298 nm for nitrogen content of 2.7 at% and linearly increase as the nitrogen content increases [74]. Our

Mossbauer measurements suggest that the martensitic phase does not contain nitrogen and that internal stress is responsible for the evolution of the lattice parameter during annealing.
Finally, we must note that significant oxidation occurs (figure 3c) after two hours of annealing, at the exact moment when the formation of the bcc phase is observed by XRD. We believe that the corrosion resistance of the nitrided stainless steel is strongly affected by this transformation that occurs for very short time of annealing (2 h.) at 400°C. Such an observation is important for industrial applications for which nitrided workpieces in austenitic stainless steel have to operate at moderate temperature (300-500°C) without losing their corrosion properties.

A recent modelling paper partially supports our conclusions [75]. Calculations, performed on the Fe-Cr-N system, show that expanded austenite can be described as an f.c.c. iron dispersively embedded with the short-range ordered clusters of type $Fe_{6-n}Cr_nN$. In the more favourable configurations, one chromium atom has more than one nitrogen atom as first neighbour [75].

5 Conclusion

The decomposition of expanded austenite formed in AISI 316LN nitrided for 4 h. at 410 °C in a UDECR device was studied by CEMS and XRD for different annealing times at 400°C.
For the as nitrided sample, the CEMS spectra show the paramagnetic contribution of austenite and two magnetic contributions. Two hyperfine field distributions (HFD A and HFD B) were used to describe the magnetic contribution. HFD A was attributed to a expanded austenite. It was shown that HFD A cannot be attributed solely to a γ' M_4N (M = Fe, Ni, Cr…) environment even if deformations induced by high internal stresses are taken into account. Our contribution is to attribute HFD B to a bcc environment. Such environment is associated to the first step for the formation of a bcc phase, ferrite or more presumably martensite without or with very low nitrogen content. The broad range of hyperfine field in HFD B can be explained by both the local deformation of the bcc lattice and by the presence of M elements as iron neighbouring atoms.
After only 2 h. of annealing, HFD A and the (200) peak of expanded austenite disappear and a bcc phase is observed by XRD. The vanishing of HFD A was explained by the diffusion of nitrogen in excess from the superficial part of the nitrided layer to the bulk during annealing. Nitrogen in excess is nitrogen not linked to chromium by short-range ordering. The occurrence of the bcc phase after 2 h. of annealing was shown to be connected to HFD B, a martensitic environment of iron with low nitrogen content or without nitrogen The interplay between local internal stress and local nitrogen content was proposed to explain the formation of a martensitic phase from the martensitic environment as detected by CEMS in the as nitrided sample. Nitrogen atoms linked to chromium by SRO must be considered as inefficient for stabilizing a gamma phase.
Our results clearly show that it does not seem relevant to consider expanded austenite as a solid solution. The nitrogen atoms are concentrated around chromium atoms in strongly or weakly linked forms, leaving in the structure areas where the iron atoms no longer undergo the influence of chromium and nitrogen. These zones are likely to give a bcc phase during annealing.

Acknowledgments

This work was supported by the French Government through the programs Institut Carnot ICÉEL, and "Investissements d'avenir" operated by the French National Research Agency (ANR) and referenced to as ANR-11-LABEX-0008-01 (LabEx DAMAS).

6 References

1) Z.L. Zhang, T. Bell, Surface Engineering, Structure and Corrosion Resistance of Plasma Nitrided Stainless Steel, 1985 1 131-136. (https://doi.org/10.1179/sur.1985.1.2.131)
2) K. Ichii, K. Fujimara, T. Takase, Structure of the ion-nitrided layer of 18-8 stainless steel, Technological Report from the Kansai University, **27** (1986) 135-144.
3) T. Czerwiec, H. He, G. Marcos, T. Thiriet, S. Weber, H. Michel, Fundamental and Innovations in Plasma Assisted Diffusion of Nitrogen and Carbon in Austenitic Stainless Steels and Related Alloys, Plasma Processes and Polymers **6 (**2009) 401-409. (https://doi.org/10.1002/ppap.200930003)
4) H. Dong, S-phase surface engineering of Fe-Cr, Co-Cr and Ni-Cr alloys, International Materials Reviews, 55 (2010) 65-98 (https://doi.org/10.1179/095066009X12572530170589).
5) J. Oddershede, T.L. Christiansen, K. Stahl, M.A.J. Somers. Scripta Mater, Extended X-ray absorption fine structure investigation of nitrogen stabilized expanded austenite, Scripta Materialia 62 (2010) 290-293.(http://dx.doi.org/10.1016/j.scriptamat.2009.11.021)
6) A. Martinavicius, G. Abrasonis, A.C. Scheinost, R. Danoix, F. Danoix, J.C. Stinville, G. Talut, C. Templier, O. Liedke, S. Gemming, W. Möller, Nitrogen interstitial diffusion induced decomposition in AISI 304L austenitic stainless steel, Acta Materialia 60 (2012) 4065–4076. (http://dx.doi.org/10.1016/j.actamat.2012.04.014)
7) X. Xu, L. Wang, Z. Yu, J. Qiang, Z. Hei, Study of microstructure of low-temperature plasma-nitrided AISI 304 stainless steel, Met. Mat. Trans. A, 31a (2000), 1193-1199. (https://doi.org/10.1007/s11661-000-0115-1)
8) X. Xu, L. Wang, Z. Yu, Z. Hei, A comparative study on microstructure of the plasma-nitrided layers on austenitic stainless steel and pure Fe, Surf. Coat. Technol., 192 (2005) 220-224. (http://dx.doi.org/10.1016/j.surfcoat.2004.04.085)
9) D. Stroz, M. Psoda, TEM studies of plasma nitrided austenitic stainless steel, J. of Microscopy, 237 (2010) 227-231. (https://doi.org/10.1111/j.1365-2818.2009.03228.x)
10) O. Ozturk, D.L. Williamson, Phase and composition depth distribution analyses of low energy, high flux N implanted stainless steel, J. Appl. Phys., 77 (1995) 3839-3850. (https://doi.org/10.1063/1.358561)
11) M. P. Fewell, D. R. G. Mitchell, J. M. Priest, K. T. Short, and G. A. Collins, The nature of expanded austenite, Surf. Coat. Technol. 131 (2000), 300-306. (http://dx.doi.org/10.1016/S0257-8972(00)00804-5)
12) M. Olzon-Dionysio, S.D. de Souza, R.L.O. Basso, S. de Souza, Application of Mössbauer spectroscopy to the study of corrosion resistance in NaCl solution of plasma nitrided AISI 316L stainless steel, Surf. Coat. Technol. 202 (2008) 3607–3614. (https://doi.org/10.1016/j.surfcoat.2007.12.040)
13) R. L. O. Basso, V. L. Pimentel, S. Weber, G. Marcos, T. Czerwiec, I. J. R. Baumvol, C. A. Figueroa, Magnetic and structural properties of ion nitrided stainless steel, J. Appl. Phys. 105, (2009) 124914-124914-5 . (https://doi.org/10.1063/1.3153945)
14) R Leutenecker, G Wagner, T Louis, U Gonser, L Guzman, Phase transformations of a nitrogen-implanted austenitic stainless steel (X10 CrNiTi 18-9), Materials Science and Engineering, A ll 5 (1989) 229-244. (https://doi.org/10.1016/0921-5093(89)90684-9)
15) M. Hillert, J. Ågren, On the definitions of paraequilibrium and orthoequilibrium, Scripta Materialia, 50 (2004) 697-699. (https://doi.org/10.1016/j.scriptamat.2003.11.020)

16) G.M. Michal, F. Ernst, and A.H. Heuer, Carbon paraequilibrium in austenitic stainless steel, Met. Mat. Trans. A, 37a (2006) 1819-1824. (https://doi.org/10.1007/s11661-006-0124-9)
17) A. Lacoste, T. Lagarde, S. Bechu, Y. Arnal, J. Pelletier, Multi-dipolar plasmas for uniform processing: physics, design and performance, J. of Plasma Sources: Science and Technology, 2002 11 407-412. (http://dx.doi.org/10.1088/0963-0252/11/4/307)
18) G. Le Caer, J. M. Dubois, Evaluation of hyperfine parameter distributions from overlapped Mossbauer spectra of amorphous alloys, J. Phys. E: Sci. Instrum., 12 (1979) 1083-1090. (http:// /doi.org/10.1088/0022-3735/12/11/018)
19) J. Hesse and A. Riibartsch, Model independent evaluation of overlapped Mossbauer spectra, J. Phys. E 7 (1974) 526-532. (http://doi.org/10.1088/0022-3735/7/7/012)
20) J.P. Eymery, N. Merakeb, Ph. Goudeau, A. Fnidiki, B. Bouzabata, A Mössbauer comparative study of the local environment in metastable 304 stainless steel films depending on the preparation mode, Journal of Magnetism and Magnetic Materials 256 (2003) 227–236. (http://dx.doi.org/10.1016/S0304-8853(02)00487-0)
21) D.L. Williamson, O. Ozturk, R. Wei, P.J. Wilbur, Metastable phase formation and enhanced diffusion in fcc alloys under high dose, high flux nitrogen implantation at high and low ion energies, Surface and Coating Technology, 65 (1994) 15-23. (https://doi.org/10.1016/S0257-8972(94)80003-0)
22) F.N. Jespersen, J.H. Hattel, M.A.J. Somers, Modelling the evolution of composition-and stress depth profiles in austenitic stainless steels during low-temperature nitriding, Modelling and Simulation in Materials Science and Engineering, 24 (2016) 25003. https://doi.org/10.1088/0965-0393/24/2/025003
23) T. Czerwiec, H. Michel, E. Bergmann, Low-pressure, high-density plasma nitriding: mechanisms, technology and results, Surf. Coat. Technol., 108-109 (1998) 182-190. (https://doi.org/10.1016/S0257-8972(98)00555-6)
24) J.M. Genin, J. Foct, Mössbauer spectroscopy of disordered and ordered iron–nitrogen solid solutions, Physica status solidi (a), 17 (1973) 395-406. (https://doi.org/10.1002/pssa.2210170203)
25) P.M. Gielen, R. Kaplow, Mossbauer effect in iron-carbon and iron-nitrogen alloys, Acta Metallurgica, 15 (1967) 49–63. (http://dx.doi.org/10.1016/0001-6160(67)90155-1)
26) V.M. Nadutov, Mössbauer analysis of the effect of substitutional atoms on the electronic charge distribution in nitrogen and carbon austenites, Mat. Sci. and Engi A, 254 (1998) 234-241. (http://dx.doi.org/10.1016/S0921-5093(98)00663-7)
27) P. Schaaf, Laser nitriding of metals, Progress in Mat. Sci., 47 (2002) 1-161. (https://doi.org/10.1016/S0079-6425(00)00003-7)
28) K. Oda, H. Fujimura, H. Ino, Interaction and arrangement of nitrogen atoms in FCC γ-iron, J. Phys. Cond. Matter 2 (1990), 10147-10158.
29) Ph. Bauer, C.N.O. Uwakweh, J.M. Genin, CEMS study of the carbon distribution in austenite, 41 (1988) Hyperfine Interact., 555-558. (https://doi.org/10.1007/BF02400451)
30) S. Cusenza, D. Jürgens, M. Uhrmacher, P. Schaaf, Nitrided Amorphous Stainless Steel Coatings Deposited by Reactive Magnetron Sputtering from an Austenitic Stainless Steel Target, Advanced Engineering Materials, 11 (2009) 17-25. (https://doi.org/10.1002/adem.200800228)
31) B. K. Brink, K. Ståhl, T. L. Christiansen , C. Frandsen, M. F. Hansen, M.A.J. Somers, Composition-dependent variation of magnetic properties and interstitial ordering in homogeneous expanded austenite, Acta Materialia 106 (2016) 32-39. (https://doi.org/10.1016/j.actamat.2015.12.043)
32) M. Olzon-Dionysio, D. Olzon-Dionysio, M. Campos, W.T. Shigeyosi, S. Dionysio de Souza, S. de Souza, Corrosion resistance of AISI 316L plasma nitride at different

temperatures and times, Hyperfine Interactions 240 (2019) 26 (https://doi.org/10.1007/s10751-019-1563-1)
33) J. L. Costa-Krämer, D. M. Borsa, J. M. Garcia-Martin, M. S. Martin-Gonzalez, D. O. Boerma, F. Briones, Structure and magnetism of single-phase epitaxial γ′−Fe_4N, Phys. Rev. B, 69 (2004) 144402. (https://doi.org/10.1103/PhysRevB.69.144402)
34) X.G. Diao, R.B. Scorzelli, H.R. Rechenberg, 57Fe Mössbauer study of perovskite-type Fe–Ni nitrides γ′-(Fe1− xNix) 4N (0⩽ x⩽ 0.8), Journal of Magnetism and Magnetic Materials 218 (2000) 81-90. (https://doi.org/10.1016/S0304-8853(00)00317-6)
35) R. N. Panda, G. Balaji and N. S. Gajbhiye, Enhancement of Hyperfine Fields for Iron Atoms in γ′-Fe_{4-x} Ni_x N (0.2 ≤ x ≤ 0.8) Compounds, Hyperfine Interactions, 141-142 (2002) 187–191. (http://dx.doi.org/10.1023/A:1021278709080)
36) P. Mohn, S.F. Matar, The γ-Fe_4N system revisited: an ab initio calculation study of the magnetic interactions, J. of Magnetism and Magnetic Materials, 191 (1999) 234-240. (https://doi.org/10.1016/S0304-8853(98)00312-6)
37) C. Paduani, J.C. Krause, Local magnetic properties and electronic structure of γ'-Fe_4N, J. of Magnetism and Magnetic Materials, 138 (1994) 109-114. (https://doi.org/10.1016/0304-8853(94)90406-5)
38) C.L. Yang, M.M. Abd-Elmeguid, H. Micklitz, G. Michels, J.W. Otto, Y. Kong, D.S. Xue, F.S. Li, Pressure effects on the electronic properties and the magnetic ground state of γ′-Fe_4N, J. of Magnetism and Magnetic Materials, 151 (1995) L19-L23. (https://doi.org/10.1016/0304-8853(95)00530-7)
39) F.S. Li, Y. Kong, R. Zhou, C.L. Yang, M.M. Abd-Elmeguid, G. Michels, H. Micklitz, J.W. Otto, Electronic and magnetic properties of the ferromagnetic γ′-Fe4N under high pressure, Solid State Communications, 95 (1995) 753-757. (https://doi.org/10.1016/0038-1098(95)00362-2)
40) S. El Khiraoui, M. Sajieddine, M. Vergnat, M. Sahlaoui, Ph. Bauer, M. Mabrouki, X-ray diffraction and Mössbauer study of $(Fe_{1-x}Ni_x)_4N$ (0.2 ≤ x ≤ 0.6) films, Journal of Alloys and Compounds 440 (2007) 43–45. (https://doi.org/10.1016/j.jallcom.2006.10.015)
41) D.L. Olson, Prediction of Austenitic Weld Metal Microstructure and Properties, Welding Research Suppl. (1985) 281-295.
42) V. A. Shabashov, N. V. Gavrilov, K. A. Kozlov, A. V. Makarov, S. G. Titova, and V. I. Voronin, Structure of the Surface Layers of Metastable Austenitic Stainless
Steel Nitrided in Electron Beam Plasma, The Physics of Metals and Metallography 119 (2018) 755-763 (https://doi.org/10.1134/S0031918X18080124)
43) F.S Li, J.J Sun, C.L Chien, 57Fe Mossbauer study of metastable 304 stainless steel film with BCC structure, J. of Physics: Condensed Matter, 7 (1995) 1921-1931. (http://dx.doi.org/10.1088/0953-8984/7/9/016)
44) J.-P. Eymery, N. Merakeb, Ph. Goudeau, A. Fnidiki, B. Bouzabata, A Mössbauer comparative study of the local environment in metastable 304 stainless steel films depending on the preparation mode, J. of Magnetism and Magnetic Materials 256 (2003) 227–236. (https://doi.org/10.1016/S0304-8853(02)00487-0)
45) K. Nomura, Y. Yamada, R. Tomita, T. Yajima, K. Shimizu, M. Mashlan, CEMS study of stainless steel films deposited by pulsed laser ablation of AISI 316, Czechoslovak Journal of Physics, 55 (2005) 845-852. (https://doi.org/10.1007/s10582-005-0086-y)
46) S. Cusenza, C. Borchers, E. Carpene, P. Schaaf, The Gibbs–Thomson effect in magnetron-sputtered austenitic stainless steel films, J. Phys.: Condens. Matter 19 (2007) 106211-19. (http://dx.doi.org/10.1088/0953-8984/19/10/106211)
47) N. Hayashi, I. Sakamoto, T. Takahashi, Phase transformation in helium ion irradiated 316 stainless steel, Journal of Nuclear Materials, 128–129, (1984) 756–759. (https://doi.org/10.1016/0022-3115(84)90452-5)

48) N. Mottu, M. Vayer, R. Erre, Xe and Mo ion implantation on austenitic stainless steel: structural modification, Surface and Coatings Technology, 183 (2004) 165–173. (http://dx.doi.org/10.1016/j.surfcoat.2003.09.065)
49) J. Dudognon, M. Vayer, A. Pineau, R. Erre, Phase transformation induced by classical ion implantation in austenitic stainless steel, Surf. Interface Anal. 40 (2008) 772–775. (https://doi.org/10.1002/sia.2754)
50) D. C. Cook, Strain induced martensite formation in stainless steel, Metallurgical Transactions A, 18 (1987) 201-210. (https://doi.org/10.1007/BF02825701)50Z) V. Shrinivas,
51) S. K. Varma, L. E. Murr, Deformation-induced martensitic characteristics in 304 and 316 stainless steels during room-temperature rolling, Metallurgical and Materials Transactions A, 26 (1995) 661-671; (https://doi.org/10.1007/BF02663916)
52) S. K. Varma, J. Kalyanam, L. E. Murk, V. Srinivas, Effect of grain size on deformation-induced martensite formation in 304 and 316 stainless steels during room temperature tensile testing, J. of Mat. Sci. Letters, 13 (1994) 107-111. (https://doi.org/10.1007/BF00416816)
53) H. S. Wang, J. R. Yang, H. K. D. H. Bhadeshia, Characterisation of severely deformed austenitic stainless steel wire, Mat. Sci. Technol., 21, (2005) 1323-1328. (https://doi.org/10.1179/174328405X63980)
54) A. Szymańska, D; Oleszak, A. Grabias, M. Rosiński, K. Sikorski, J. Kazior, A. Michalski, K.J. Kurzydłowski, Phase transformation in ball milled AISI 316L stainless steel powder and the microstructure of the steel obtained by its sintering, Rev. Adv. Mater. Sci, 8 (2004) 143-146. (https://doi.org/10.1179/174328405X63980)
55) N. Hashimoto, T.S. Byun, Deformation-induced martensite formation and dislocation channeling in neutron-irradiated 316 stainless steel, Journal of Nuclear Materials 367–370 (2007) 960–965. (http://dx.doi.org/10.1016/j.jnucmat.2007.03.204)
56) J. Manjanna, S. Kobayashi, Y. Kamada, S. Takahashi, H. Kikuchi, Martensitic transformation in SUS 316LN austenitic stainless steel at RT, J Mater Sci 43 (2008) 2659–2665. (http://dx.doi.org/10.1007/s10853-008-2494-4)
57) J. Manjanna, Y. Kamada, S. Kobayashi, S. Takahashi, H. Kikuchi, Ferromagnetic fraction and exchange anisotropy in SUS 316LN austenitic stainless steel due to strain-induced deformation, J. Appl. Phys., 103 (2008) 07E713-07E713-3. (https://doi.org/10.1063/1.2830831)
58) J. Sort, A. Concustell, E. Menéndez, S. Suriñach, M. D. Baró, J. Farran, J. Nogués, Selective generation of local ferromagnetism in austenitic stainless steel using nanoindentation, Applied Physics Letters 89 (2006) 032509-032509-3. (https://doi.org/10.1063/1.2227827)
59) E. Menéndez, J. Sort, M.O. Liedke, J. Fassbender, S. Suriñach, M.D. Baró, J. Nogués, Controlled generation of ferromagnetic martensite from paramagnetic austenite in AISI 316L austenitic stainless steel, Journal of Materials Research , 24 (2009) 565-573. (https://doi.org/10.1557/JMR.2009.0067)
60) A. Etienne, B. Radiguet, C. Genevois, J.-M. Le Breton, R. Valiev, P. Pareige, Thermal stability of ultrafine-grained austenitic stainless steels, Materials Science and Engineering: A, 527 (2010) 5805–5810. (http://dx.doi.org/10.1016/j.msea.2010.05.049)
61) P. Rozenak, D. Eliezer, Phase changes related to hydrogen-induced cracking in austenitic stainless steel, Acta Metallurgica 35 (1987) 2329–2340. (https://doi.org/10.1016/0001-6160(87)90081-2)
62) P. Rozenak, A. Loew, Stress distributions due to hydrogen concentrations in electrochemically charged and aged austenitic stainless steel, Corrosion Science 50 (2008) 3021–3030. (http://dx.doi.org/10.1016/j.corsci.2008.08.045)
63) X.Y. Li, Y. Sun, T. Bell, The stability of the nitrogen S-phase in austenitic stainless steel, Z. Metallkd., 90 (1999), 901-907.

64) O. Ozturk, D.L. Williamson, Thermal stability of the high-N solid-solution layer on stainless steel, Surf. Coat. Technol., 158-159, (2002) 288-294. (http://dx.doi.org/10.1016/S0257-8972(02)00185-8)
65) T.L. Christiansen, M.A.J. Somers, Decomposition kinetics of expanded austenite with high nitrogen contents, Z. Metallkd. 97 (2006) 79-88.
66) T.L. Christiansen, M.A.J. Somers, Low-temperature gaseous surface hardening of stainless steel: the current status, Int. J. Mat. Res., 100 (2009) 1361-1377. (https://doi.org/10.3139/146.110202)
67) B. Brink, K. Stahl, T.L. Christiansen, M.A.J. Somers, Thermal expansion and phase transformations of nitrogen-expanded austenite studied with in situ synchrotron X-ray diffraction, J. Appl. Cryst., 47 (2014) 819-826. (https://doi.org/10.1107/S1600576714005214)
68) D.H. Jack, The structure of nitrided iron-titanium alloys, Acta Metall., 24 (1976) 137-146. (http://dx.doi.org/10.1016/0001-6160(76)90016-X)
69) D.S. Rickerby, S. Henderson, A. Hendry, K.H. Jack, Structure and thermochemistry of nitrided iron-titanium alloys, Acta Metall., 34 (1986) 1687-1699. (https://doi.org/10.1016/0001-6160(86)90116-1)
70) D.S. Rickerby, A. Hendry, K.H. Jack, Low-temperature aging of nitrided Fe Ti alloys, Acta Metall., 34 (1986) 1925-1932. (https://doi.org/10.1016/0001-6160(86)90251-8)
71) B. K. Brink, K. Ståhl, T. L. Christiansen, J. Oddershede, G. Winther, M.A.J. Somers, On the elusive crystal structure of expanded austenite Scripta Materialia 131 (2017) 59–62. (https://doi.org/10.1016/j.scriptamat.2017.01.006)
72) R. Abbaschian, L. Abbaschian, R. E. Reed-Hill, "Physical Metallurgy Principles", 2009, 1994 Cengage Learning.
73) L. Zwell, D. E. Carnahan, G. R. Speich, Lattice parameter of ferritic and martensitic Fe−Ni alloys, Met. Trans., 1 (1970) 1007-1009. (https://doi.org/10.1007/BF02811785)
74) O.D. Sherby, J. Wadsworth, D.R. Lesuer, C.K. Syn, Revisiting the structure of martensite in iron-carbon steels, Mat. Trans., 49 (2008) 2016-2027. (https://doi.org/10.2320/matertrans.MRA2007338)
75) K. Tong, F. Ye, Y. K. Wang, Short-range ordered structure and phase stability of supersaturated nitrided layer on austenitic stainless steel, Acta Materialia 175 (2019) 314-323. (https://doi.org/10.1016/j.actamat.2019.06.019)

Legends

Table 1: Hyperfine parameters and relative abundance of identified sub-spectra for the CEMS spectra presented in figure 3.

Figure 1 : Schematic illustration of the possible arrangements of nitrogen atoms in stainless steels: (a) 3 dimensional view of nitrogen in solid solution with a statistical distribution, (b) same in 2D, (c) short range order of nitrogen with chromium, (d) non ordered concentration of nitrogen (clusters), (e) ordered concentration zones leading to coherent precipitates of CrN or (f) Fe_xN_{1-x} and (g) one dimensional Guinier-Preston zones. For the 3 D view, the atomic compositions are 25% for N, 47 % for Fe, 14% for Cr and 14 % for other atoms. For 2D view, the atomic composition is not respected.

Figure 2 : CEMS spectrum of a non nitrided AISI 316L sample.

Figure 3 : CEMS spectra of an AISI 316L sample nitrided for 4 h. at 410° C and then annealed at 400 °C for different times : (a) as nitrided, (b) annealed for 1 h., (c) annealed for 2 h., (d) annealed for 3 h., (e) annealed for 8 h. and (f) annealed for 8 h. at 400°C and then for 5 h. at 470 °C. The given annealing times are cumulated times. The paramagnetic phase is indicated by the red curve.

Figure 4 : GDOES profiles of nitrogen content for the AISI 316L sample nitrided for 4 h. at 410° C before and the end of the annealing process (annealed for 8 h. at 400°C and then for 5 h. at 470 °C). The insert represent the evolution of the difference between N and Cr content as a function of depth.

Figure 5 : X-ray diffraction patterns of an AISI 316L sample nitrided for 4 h. at 410° C and then annealed at 400 °C for different times (same as figure 3).

Figure 6 : Evolution of the different lattice parameters calculated from the X-ray diffraction patterns of an AISI 316L sample nitrided for 4 h. at 410° C and then annealed at 400 °C for different times (same as figure 3).

Figure 7: Schematic view of atomic arrangement in the γ' structure

Figure 8: Two dimensional schematic view of atomic arrangement in expanded austenite

Experiment	Phases													
	γ		HFD A			HFD B			α or α'			Fe_3O_4		
	Isomer shift ($mm.s^{-1}$)	Relative abondance	Hyperfine field (T)	Isomer Shift ($mm.s^{-1}$)	Relative abondance	Hyperfine field (T)	Isomer Shift ($mm.s^{-1}$)	Relative abondance	Hyperfine field (T)	Isomer Shift ($mm.s^{-1}$)	Relative abondance	Hyperfine field (T)	Isomer Shift ($mm.s^{-1}$)	Relative abondance
Non nitrided	- 0.1	100%												
Nitrided 4 h. at 400°C	- 0.16	4 %	10 to 28	0.27 to 0.293	44.6 %	14.5 to 32.6	- 0.009 to 0.075	51.4 %						
Annealed 1 h. at 400°C	- 0.12	3 %	10 to 28	0.27 to 0.315	26.8 %	15 to 32.5	- 0.009 to 0.053	70.2 %						
Annealed 2 h. at 400°C	- 0.12	4 %				15 to 35.4	- 0.117 to 0.039	80 %				48.8	0.363	8 %
												46.2	0.783	8 %
Annealed 3 h. at 400°C	- 0.11	3.4 %				15 to 34.6	0.005 to 0.041	71 %	34	- 0.06	14.5 %	48	0.362	5.3 %
												46.2	0.742	5.8 %
Annealed 8 h. at 400°C	- 0.11	3.4 %				15 to 34.8	- 0.012 to 0.05	64.4 %	34	0.002	21.2 %	48	0.362	5.3 %
												46	0.742	5.7 %
Annealed 8 h. at 400°C + 5 h. at 470 °C	- 0.08	47%							34.3	- 0.06	15			
									33.3	- 0.06	28			

Table 1

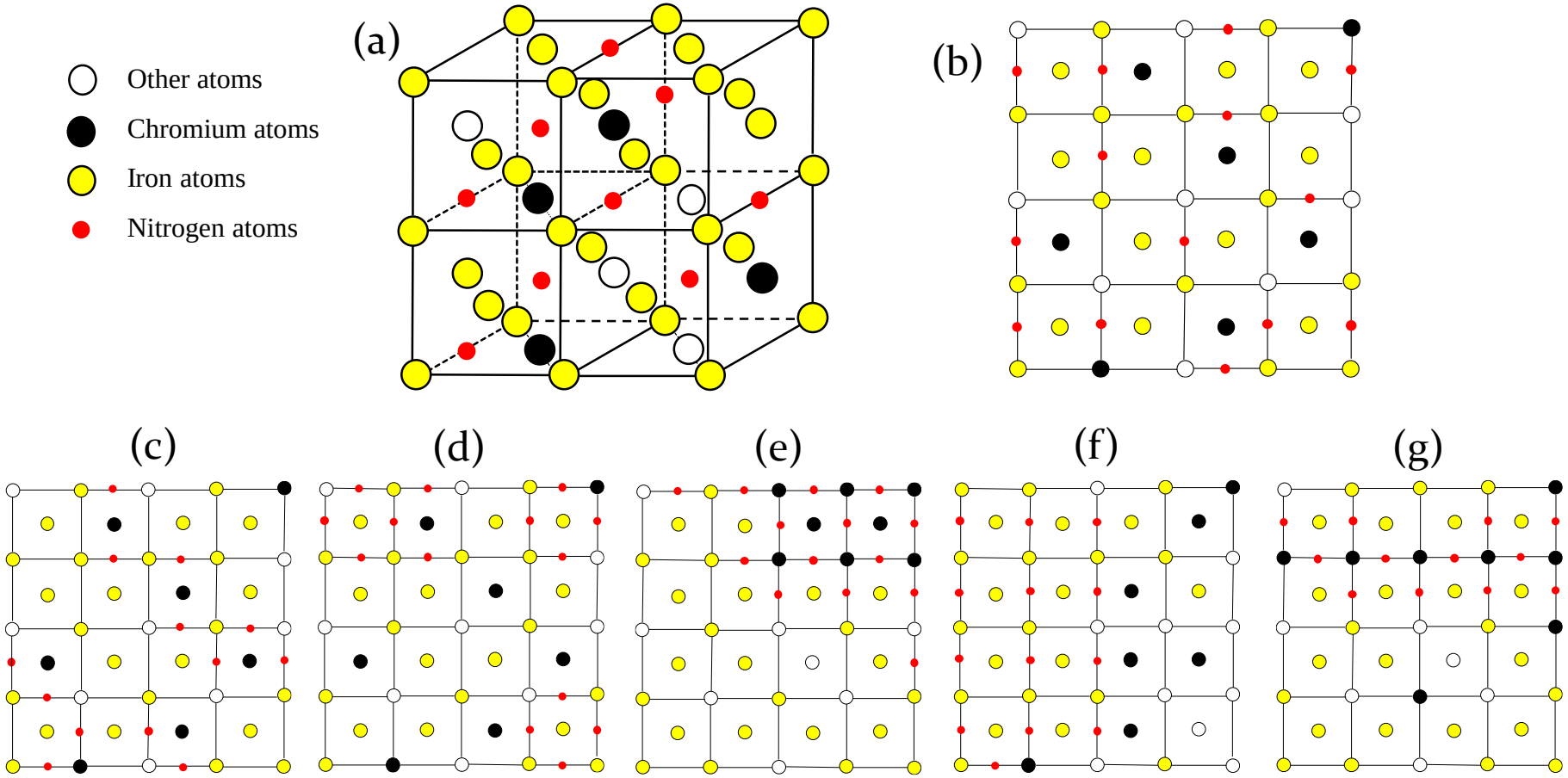
Other atoms
Chromium atoms
Iron atoms
Nitrogen atoms
(a)
(b)
(c)
(d)
(e)
(f)
(g)

Figure 1

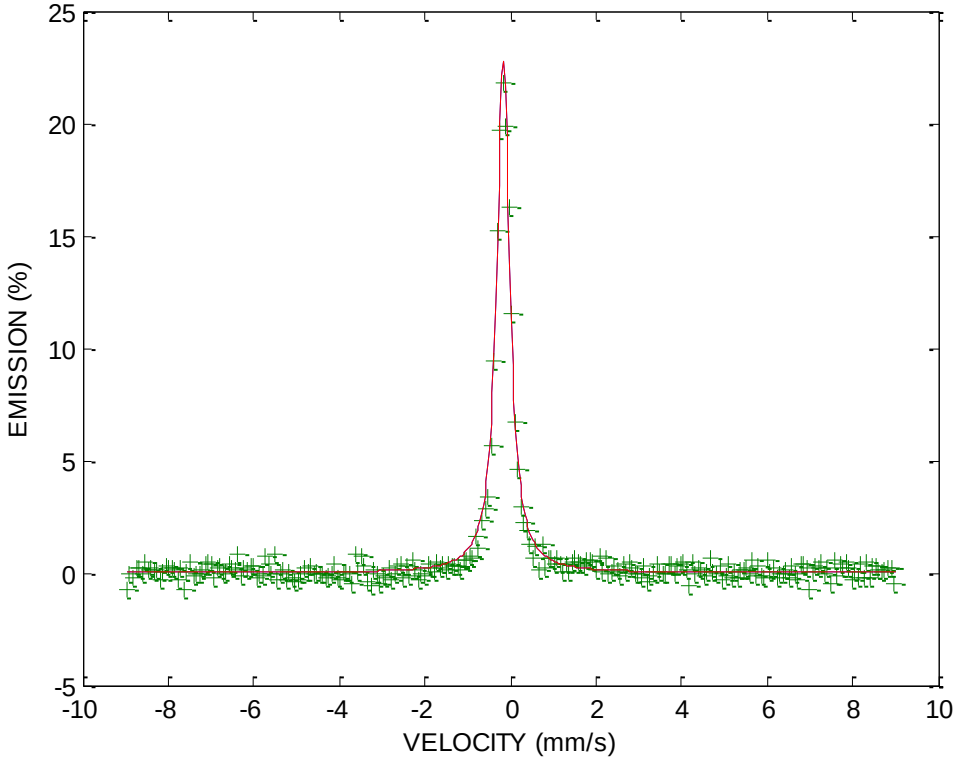

Figure 2

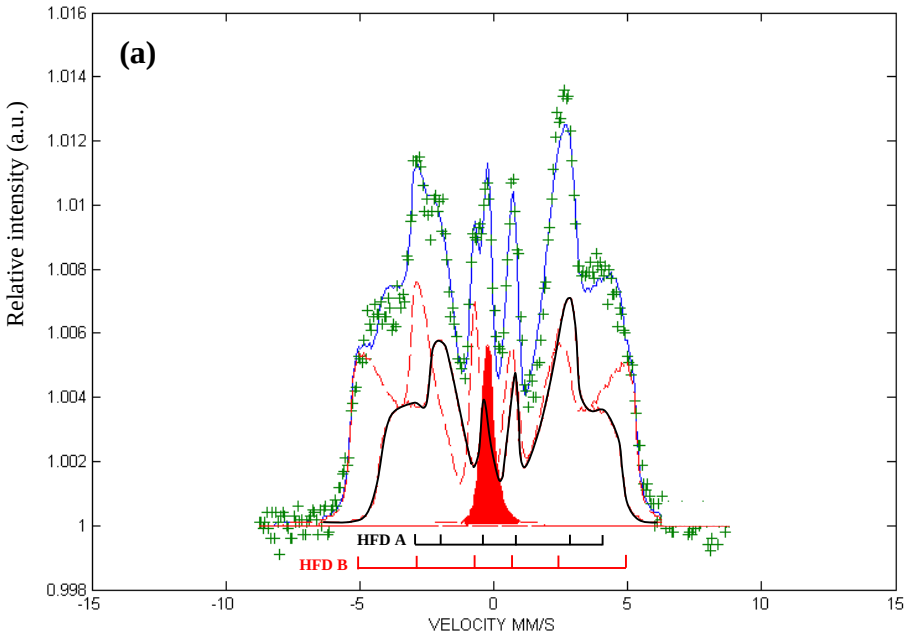
(a)
Relative intensity (a.u.)
VELOCITY MM/S
HFD A
HFD B

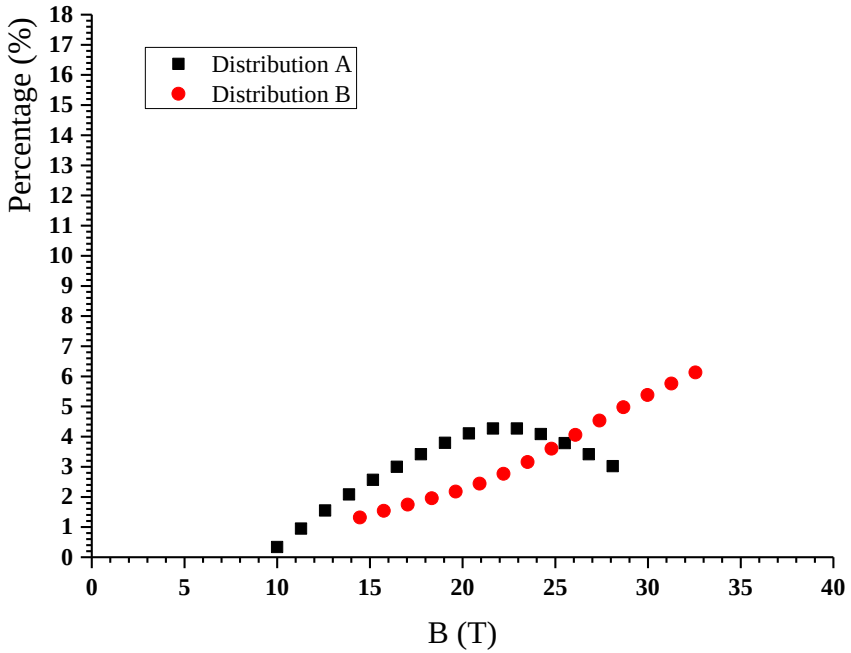
Distribution A
Distribution B
Percentage (%)
B (T)

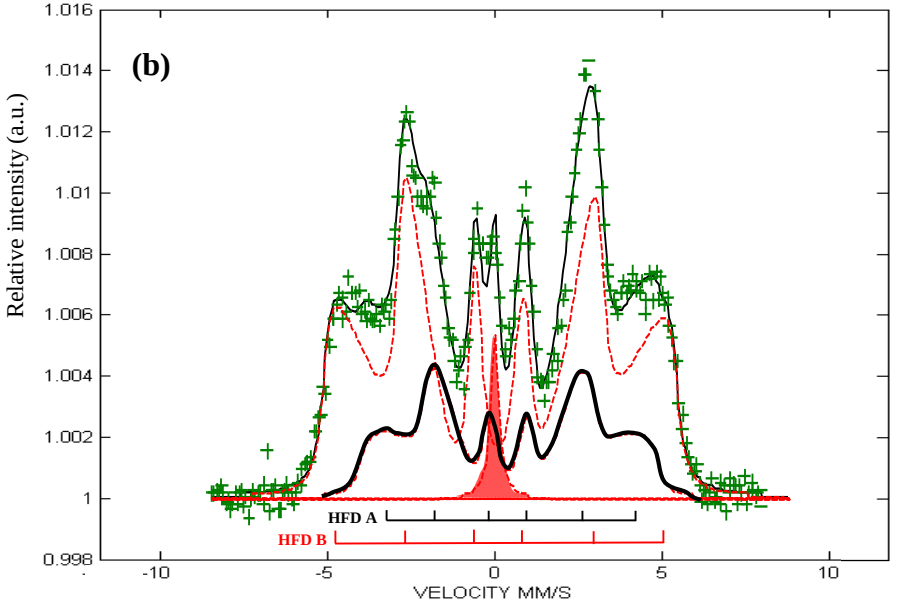
(b)
Relative intensity (a.u.)
VELOCITY MM/S
HFD A
HFD B

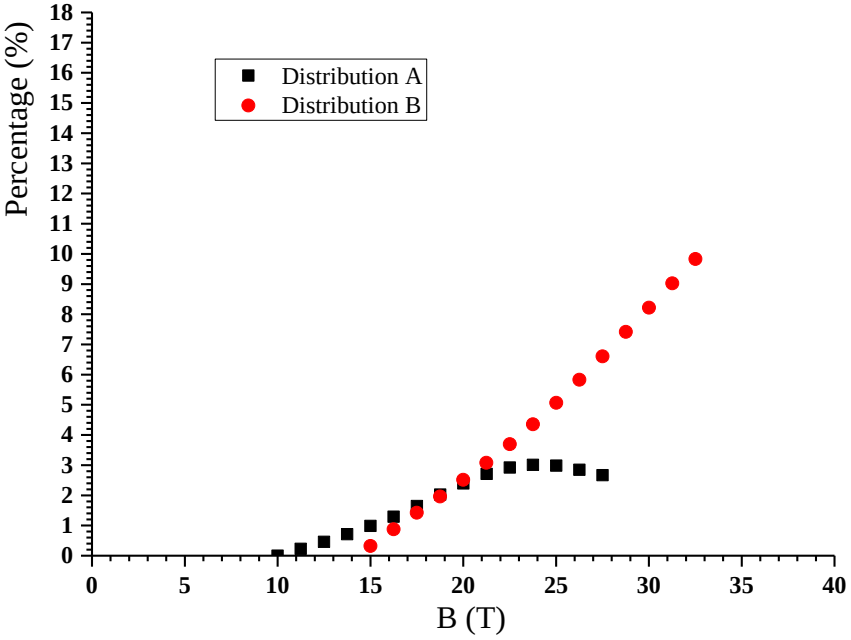
Distribution A
Distribution B
Percentage (%)
B (T)

Figure 3

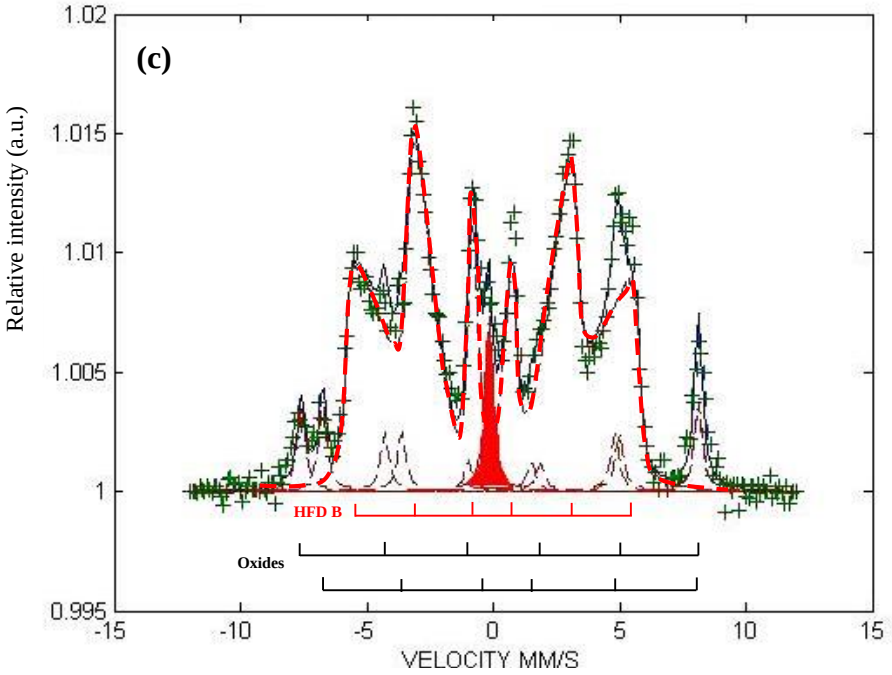
(c)
Relative intensity (a.u.)
VELOCITY MM/S
HFD B
Oxides

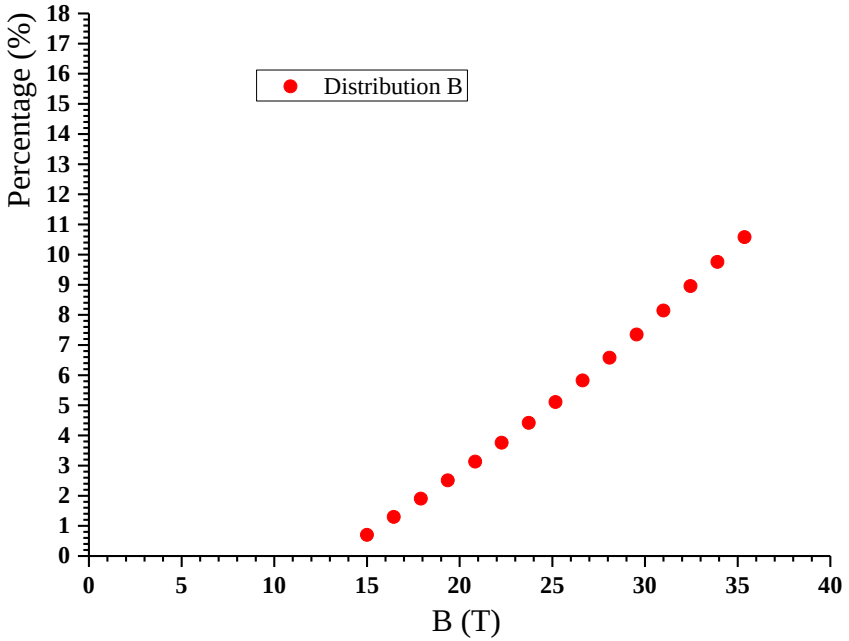
Distribution B
Percentage (%)
B (T)

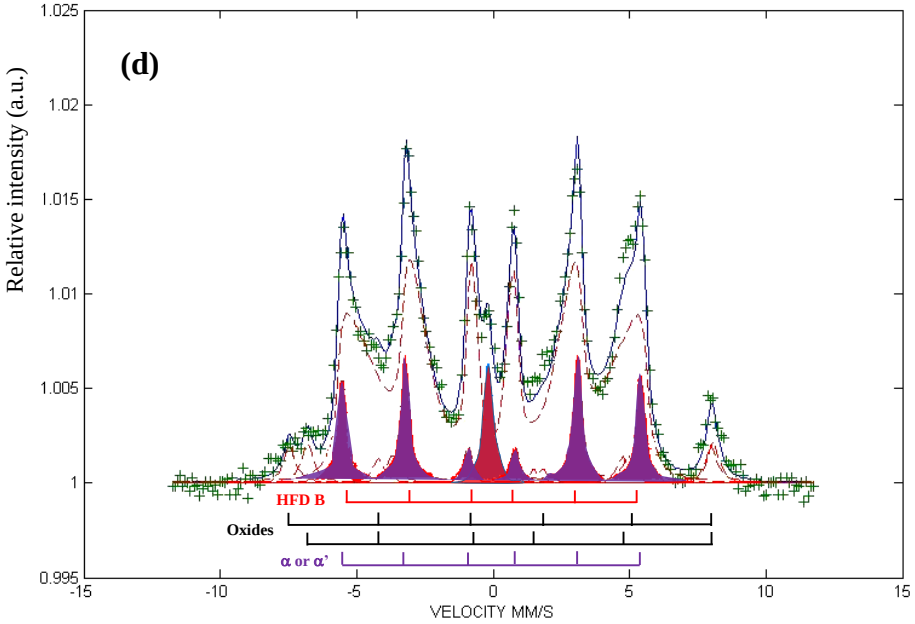
(d)
Relative intensity (a.u.)
VELOCITY MM/S
HFD B
Oxides
α or α'

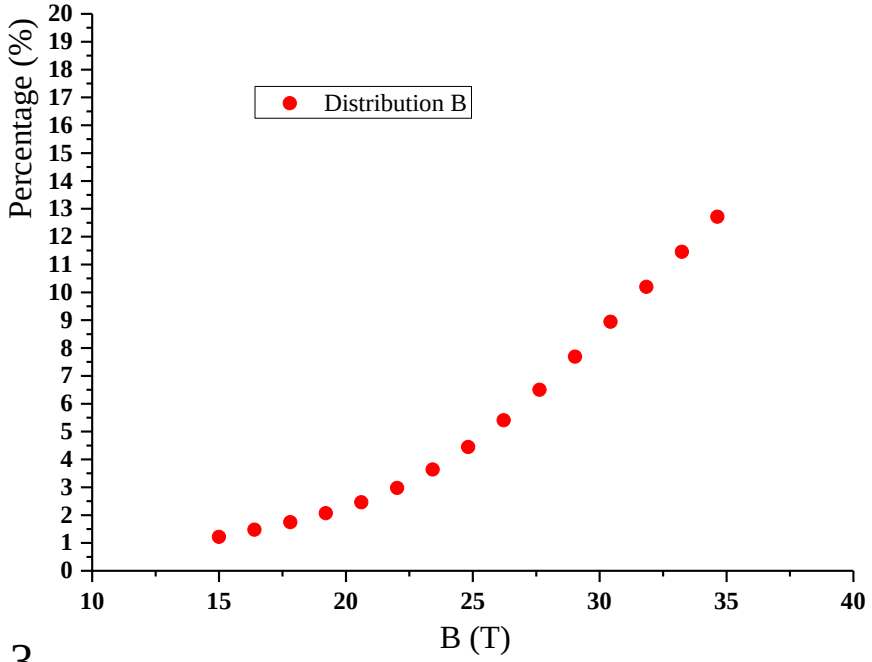
Distribution B
Percentage (%)
B (T)

Figure 3

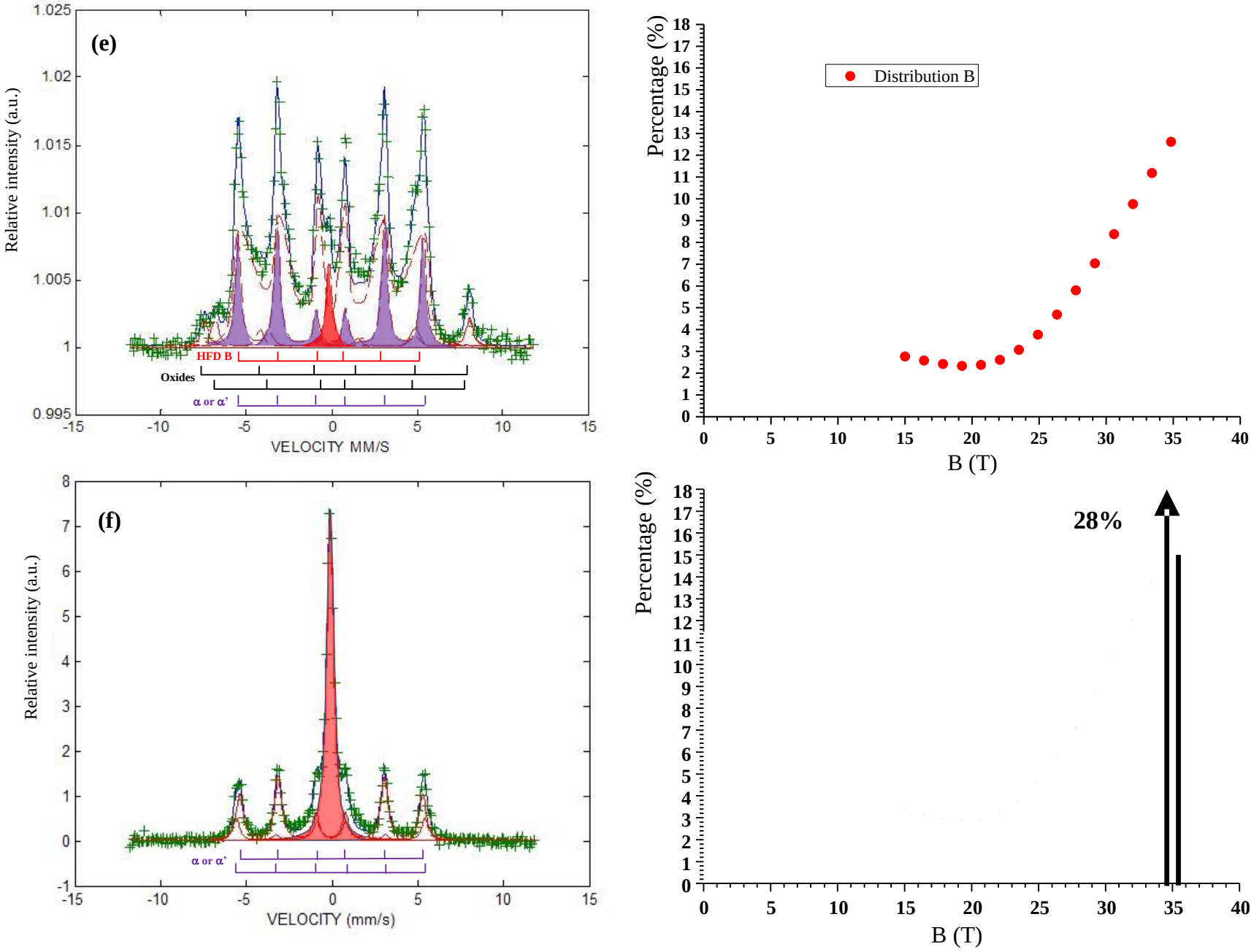
(e)
Relative intensity (a.u.)
VELOCITY MM/S
HFD B
Oxides
α or α'
Distribution B
Percentage (%)
B (T)
(f)
Relative intensity (a.u.)
VELOCITY (mm/s)
α or α'
28%
Percentage (%)
B (T)

Figure 3

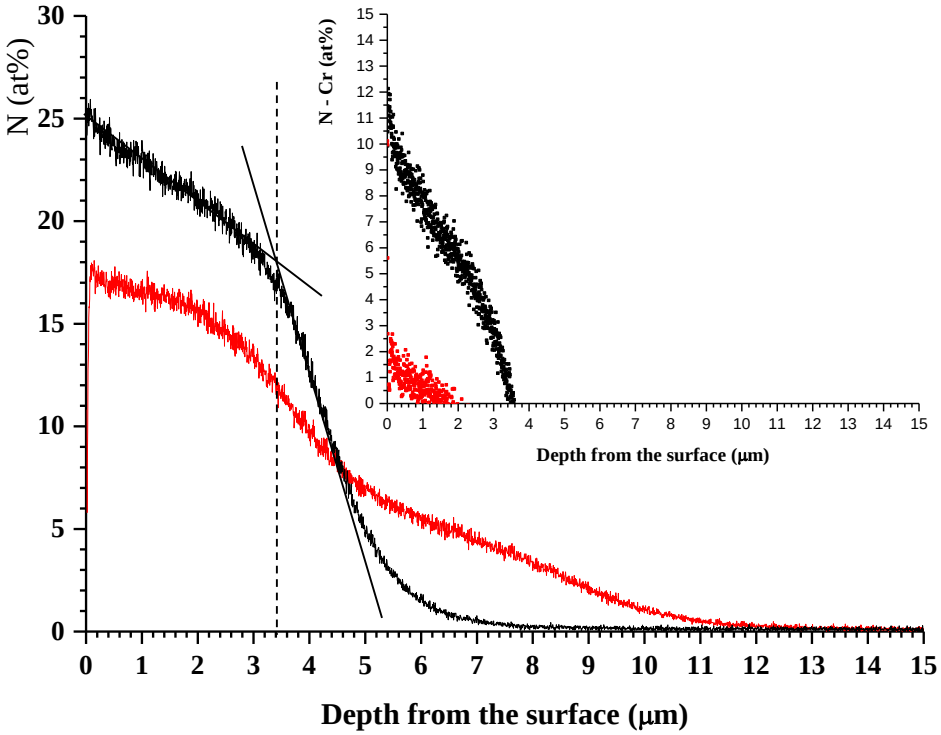
N (at%)
Depth from the surface (μm)
N - Cr (at%)
Depth from the surface (μm)

Figure 4

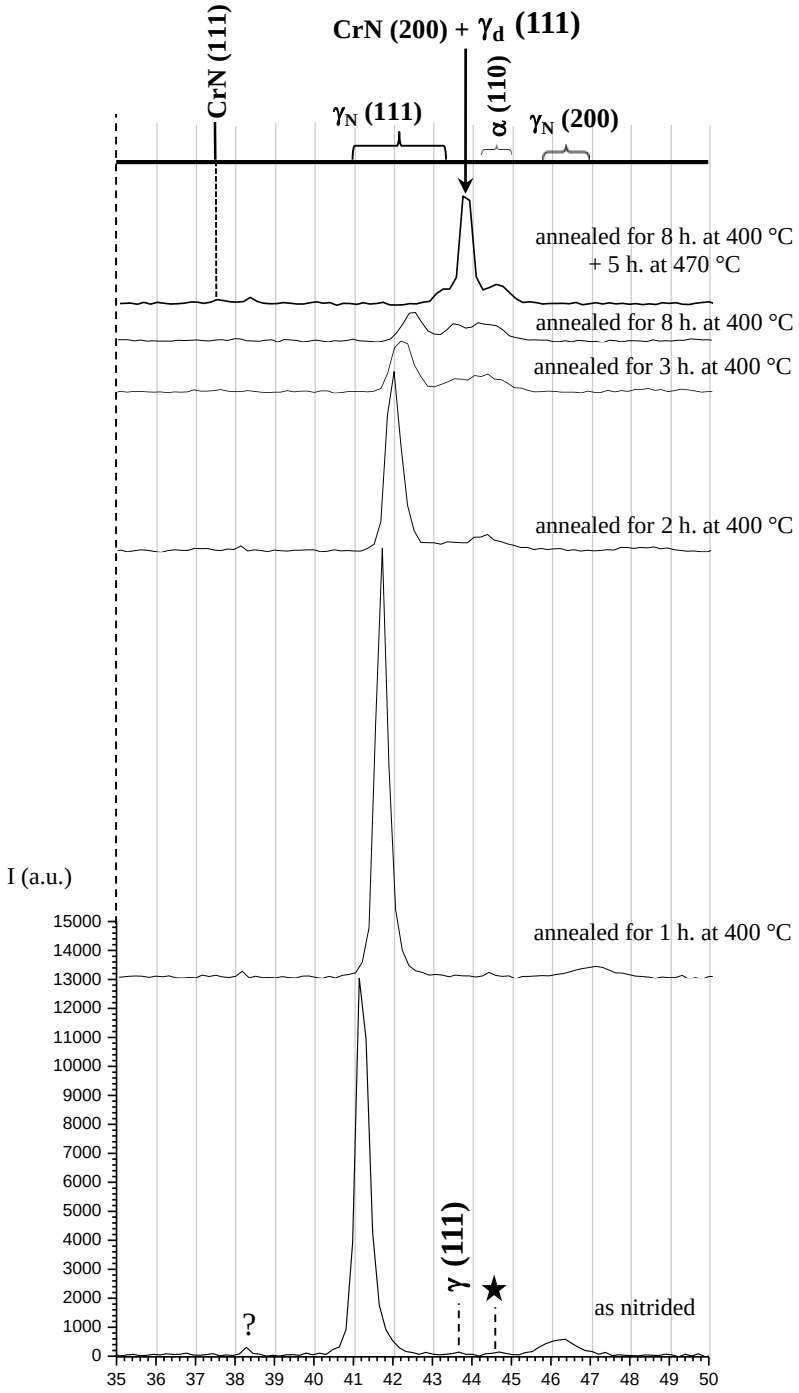
CrN (111)
CrN (200) + γd (111)
γN (111)
α (110)
γN (200)
annealed for 8 h. at 400 °C
+ 5 h. at 470 °C
annealed for 8 h. at 400 °C
annealed for 3 h. at 400 °C
annealed for 2 h. at 400 °C
annealed for 1 h. at 400 °C
as nitrided
I (a.u.)
γ (111)
?
15000
14000
13000
12000
11000
10000
9000
8000
7000
6000
5000
4000
3000
2000
1000
0
35 36 37 38 39 40 41 42 43 44 45 46 47 48 49 50

Figure 5

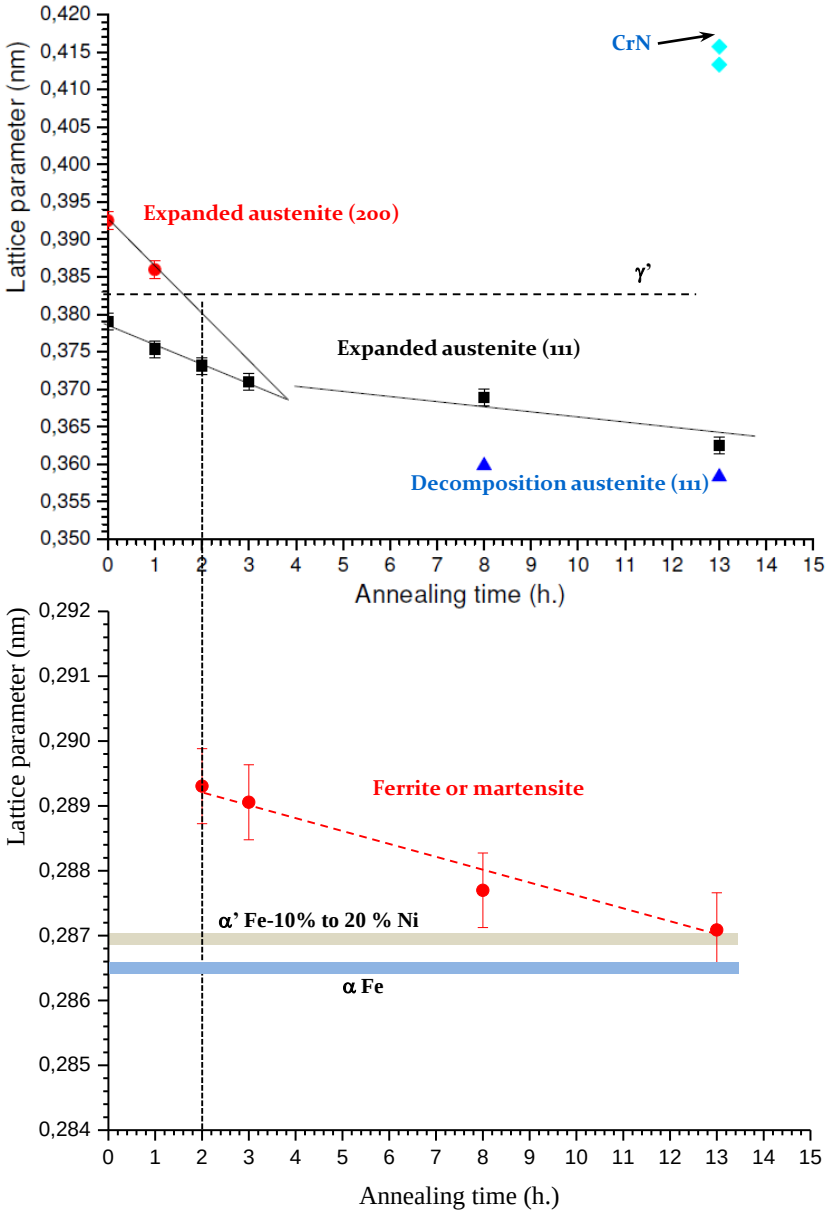
Lattice parameter (nm)
0,420
0,415
0,410
0,405
0,400
0,395
0,390
0,385
0,380
0,375
0,370
0,365
0,360
0,355
0,350
CrN
Expanded austenite (200)
γ'
Expanded austenite (111)
Decomposition austenite (111)
0 1 2 3 4 5 6 7 8 9 10 11 12 13 14 15
Annealing time (h.)
Lattice parameter (nm)
0,292
0,291
0,290
0,289
0,288
0,287
0,286
0,285
0,284
Ferrite or martensite
α' Fe-10% to 20 % Ni
α Fe
0 1 2 3 4 5 6 7 8 9 10 11 12 13 14 15
Annealing time (h.)

Figure 6

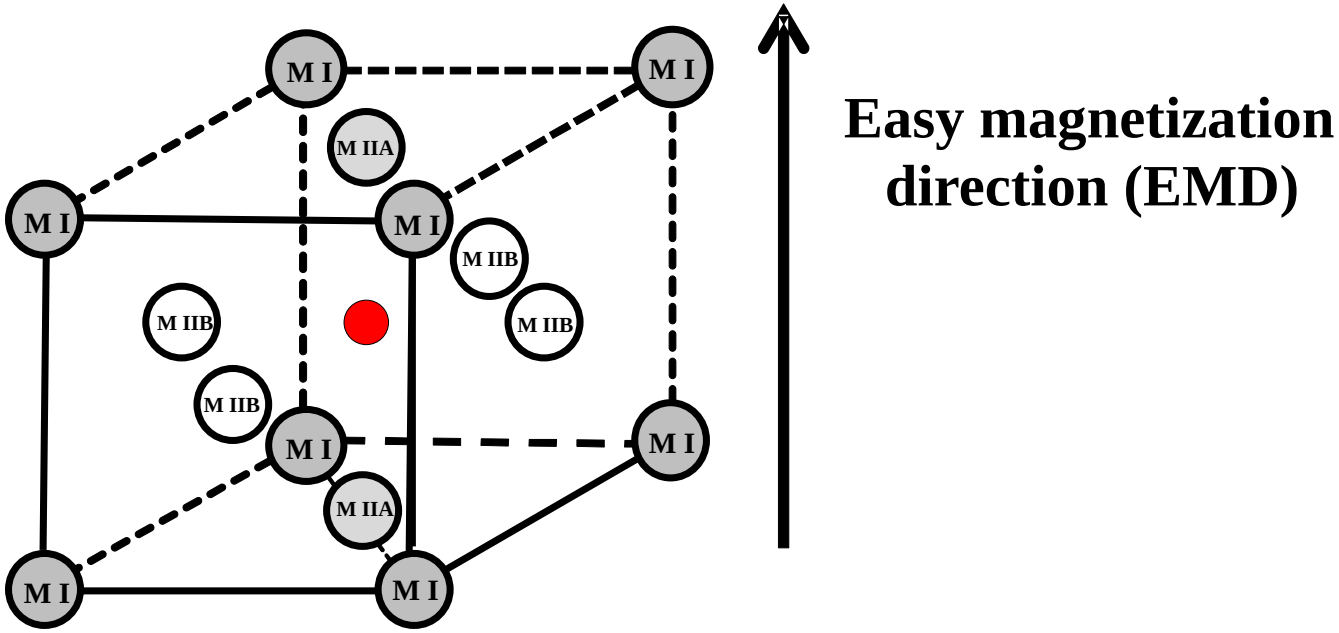
M I
M I
M IIA
M I
M I
M IIB
M IIB
M IIB
M IIB
M I
M I
M IIA
M I
M I
M
Easy magnetization direction (EMD)

Figure 7

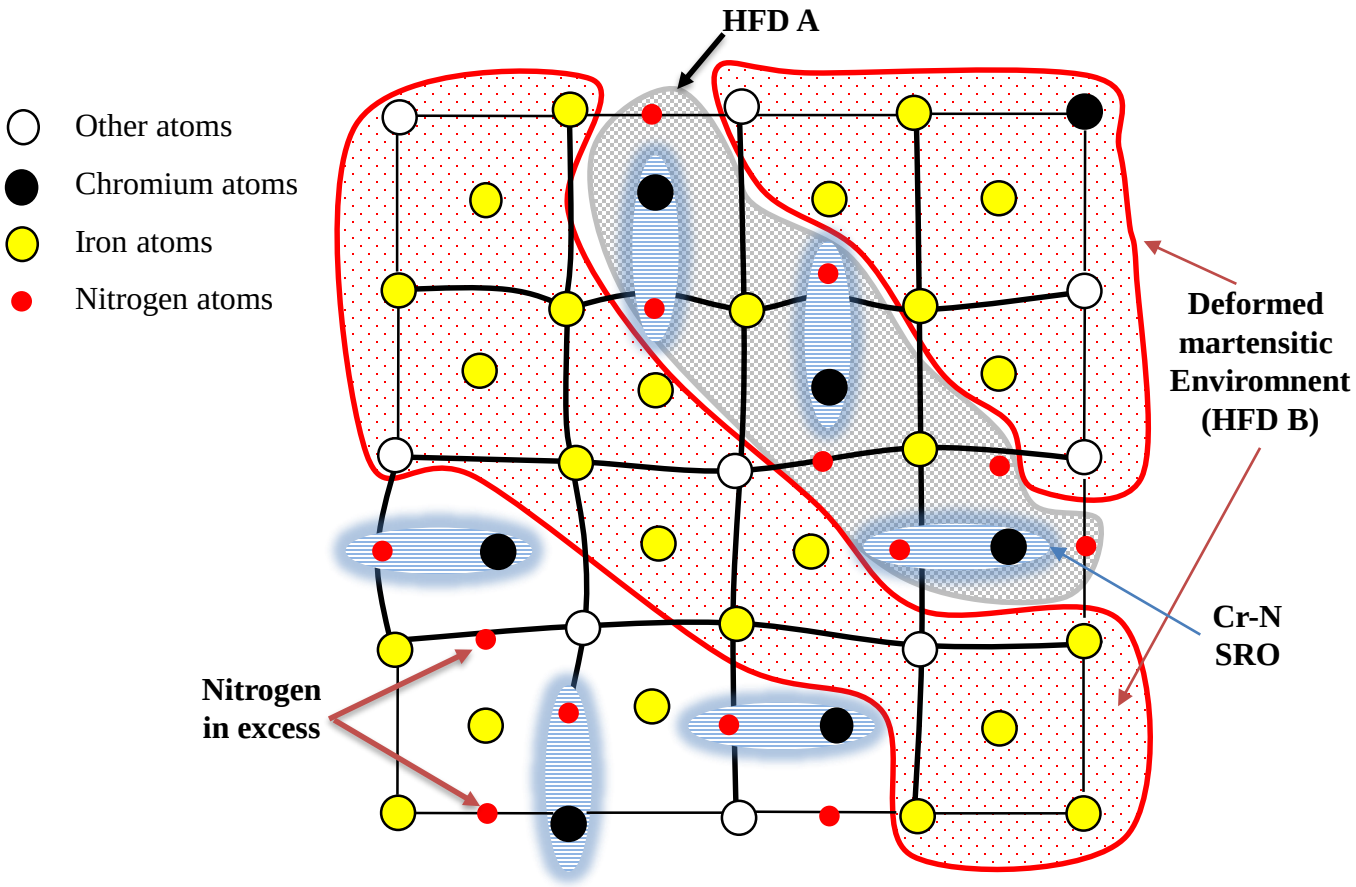
Other atoms
Chromium atoms
Iron atoms
Nitrogen atoms
HFD A
Deformed martensitic Enviromnent (HFD B)
Cr-N SRO
Nitrogen in excess

Figure 8

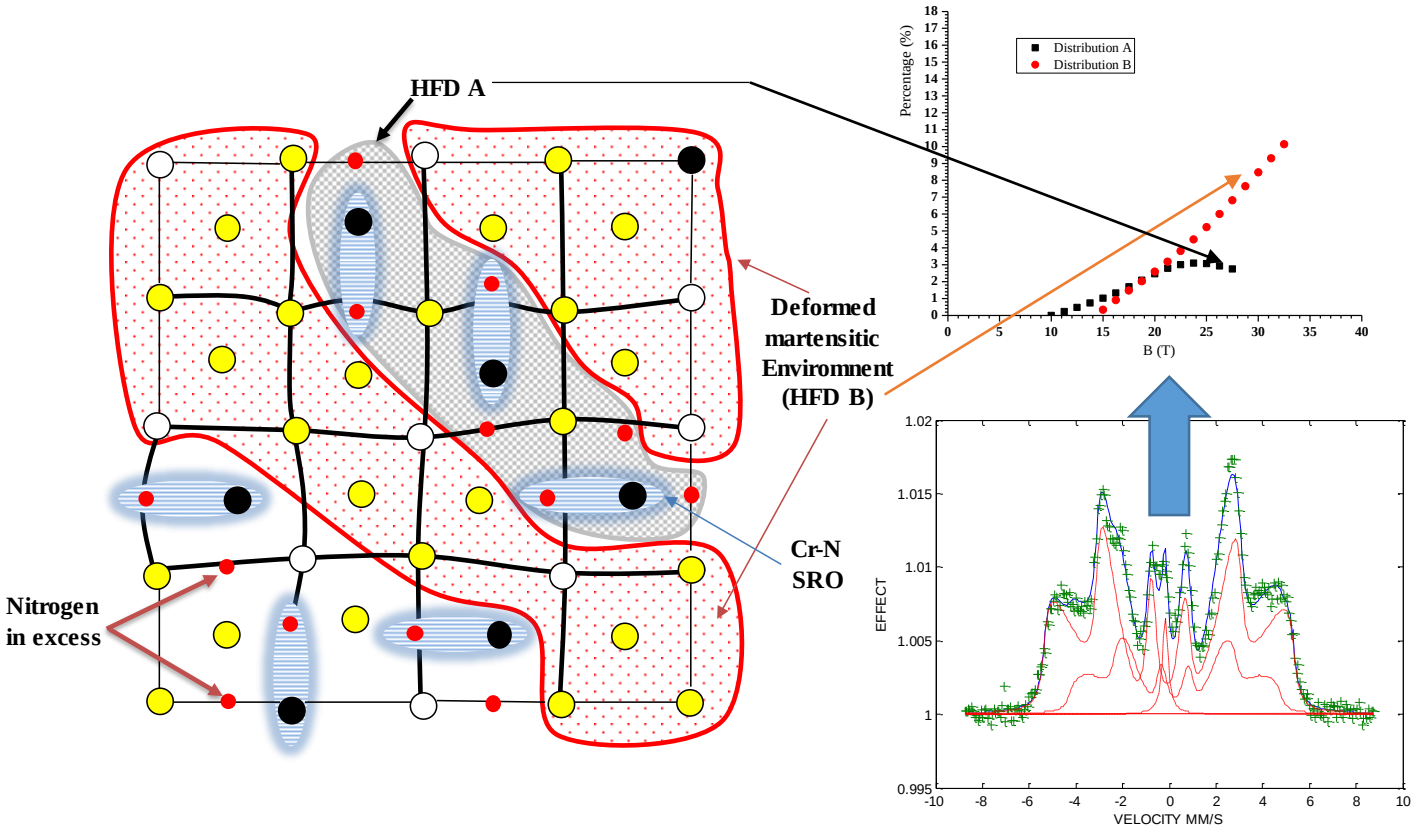
HFD A
Deformed
martensitic
Environment
(HFD B)
Cr-N
SRO
Nitrogen
in excess
Distribution A
Distribution B
Percentage (%)
B (T)
EFFECT
VELOCITY MM/S